

## From Linear Molecular Chains to Extended Polycyclic Networks: Polymerization of Dicyanoacetylene

Huiyang Gou, Li Zhu, Haw-Tyng Huang, Arani Biswas, Derek W. Keefer, Brian L Chaloux, Clemens Prescher, Liuxiang Yang, Duck Young Kim, Matthew D Ward, Jordan Lerach, Shengnan Wang, Artem R Oganov, Albert Epshteyn, John V Badding, and Timothy A. Strobel

*Chem. Mater.*, **Just Accepted Manuscript** • DOI: 10.1021/acs.chemmater.7b01446 • Publication Date (Web): 26 Jun 2017

Downloaded from <http://pubs.acs.org> on June 26, 2017

### Just Accepted

“Just Accepted” manuscripts have been peer-reviewed and accepted for publication. They are posted online prior to technical editing, formatting for publication and author proofing. The American Chemical Society provides “Just Accepted” as a free service to the research community to expedite the dissemination of scientific material as soon as possible after acceptance. “Just Accepted” manuscripts appear in full in PDF format accompanied by an HTML abstract. “Just Accepted” manuscripts have been fully peer reviewed, but should not be considered the official version of record. They are accessible to all readers and citable by the Digital Object Identifier (DOI®). “Just Accepted” is an optional service offered to authors. Therefore, the “Just Accepted” Web site may not include all articles that will be published in the journal. After a manuscript is technically edited and formatted, it will be removed from the “Just Accepted” Web site and published as an ASAP article. Note that technical editing may introduce minor changes to the manuscript text and/or graphics which could affect content, and all legal disclaimers and ethical guidelines that apply to the journal pertain. ACS cannot be held responsible for errors or consequences arising from the use of information contained in these “Just Accepted” manuscripts.

# From Linear Molecular Chains to Extended Polycyclic Networks: Polymerization of Dicyanoacetylene

Huiyang Gou,<sup>1,2,\*†</sup> Li Zhu<sup>1,\*</sup>, Haw-Tyng Huang,<sup>3</sup> Arani Biswas,<sup>3</sup> Derek W. Keefer,<sup>3</sup> Brian L. Chaloux,<sup>4</sup> Clemens Prescher,<sup>5</sup> Liuxiang Yang,<sup>1,2</sup> Duck Young Kim,<sup>1,2</sup> Matthew D. Ward,<sup>1</sup> Jordan Lerach,<sup>3</sup> Shengnan Wang,<sup>6</sup> Artem R. Oganov,<sup>7,6</sup> Albert Epshteyn,<sup>8</sup> John V. Badding,<sup>3</sup> Timothy A. Strobel<sup>1,‡</sup>

<sup>1</sup>Geophysical Laboratory, Carnegie Institution of Washington, Washington, DC 20015, USA

<sup>2</sup>Center for High Pressure Science and Technology Advanced Research, Beijing 100094, China.

<sup>3</sup>Department of Chemistry, Department of Physics, Department of Materials Science and Engineering, and Materials Research Institute, The Pennsylvania State University, University Park, PA 16802, USA.

<sup>4</sup>NRC Postdoctoral Associate, Naval Research Laboratory, 4555 Overlook Ave., SW, Washington, DC 20375, USA

<sup>5</sup>Center for Advanced Radiation Sources, University of Chicago, Argonne, IL 60437, USA

<sup>6</sup>Department of Geosciences, Center for Materials by Design, and Institute for Advanced Computational Science, State University of New York, Stony Brook, NY 11794-2100

<sup>7</sup>Skolkovo Institute of Science and Technology, Skolkovo Innovation Center, 3 Nobel St., Moscow 143026, Russia.

<sup>8</sup>Naval Research Laboratory, Washington, DC20375, USA

\*Contributed equally to this work

†huiyang.gou@hpstar.ac.cn

‡tstrobel@ciw.edu

## ABSTRACT

Dicyanoacetylene (C<sub>4</sub>N<sub>2</sub>) is an unusual energetic molecule with alternating triple and single bonds (think miniature, nitrogen-capped carbyne), which represents an interesting starting point for the transformation into extended carbon-nitrogen solids. While pressure-induced polymerization has been documented for a wide variety of related molecular solids, precise mechanistic details of reaction pathways are often poorly understood and the characterization of recovered products is typically incomplete. Here, we study the high-pressure behavior of C<sub>4</sub>N<sub>2</sub> and demonstrate polymerization into a disordered carbon-nitrogen network that is recoverable to ambient conditions. The reaction proceeds via activation of linear molecules into buckled molecular chains, which spontaneously assemble into a polycyclic network that lacks long-range order. The recovered product was characterized using a variety of optical spectroscopies, X-ray methods and theoretical simulations, and is described as a predominately *sp*<sup>2</sup> network comprising “pyrrolic” and “pyridinic” rings with an overall tendency towards a two-dimensional structure. This understanding offers valuable mechanistic insights into design guidelines for next-generation carbon nitride materials with unique structures and compositions.

## INTRODUCTION

Carbon nitride materials have attracted continuous attention in research over past decades as indicated by extensive efforts from both theory<sup>1-2</sup> and experiments<sup>3-19</sup>. Sustained interest in nitrogen-bearing, carbon-rich materials stems from their multiple functionalities and diverse applications.<sup>1-19</sup> For example, cubic carbon nitride (*c*-C<sub>3</sub>N<sub>4</sub>) is predicted to have comparable hardness to diamond,<sup>1-2</sup> whereas graphitic carbon nitride (*g*-C<sub>3</sub>N<sub>4</sub>) has been demonstrated to act as a photocatalyst for various redox reactions.<sup>4-19</sup> Furthermore, nitrogen-doped carbon materials often exhibit excellent properties as compared with their pure carbon counterparts, *e.g.* conductivity, basicity, oxidation stability, and catalytic activity, although these properties are highly dependent on the amount of nitrogen incorporated within the structure.<sup>4-19</sup> When long-range order within carbon nitride materials is lacking, disordered structures containing *sp*<sup>2</sup> and *sp*<sup>3</sup> bonding may still exhibit outstanding mechanical properties,<sup>20-26</sup> which is fundamentally important for the realization of three-dimensional, crystalline carbon nitride solids.

Previous attempts to produce novel CN solids have largely revolved around varying deposition methods to manipulate particle size and texture, together with control of nitrogen content.<sup>10-17</sup> Nevertheless, adventitious hydrogen incorporation within these materials limits the development of structure-property relationships for precise stoichiometries and diverse CN building blocks.<sup>27-32</sup> High-energy molecules can provide an alternative path towards the formation of unique structures, and high-pressure chemistry may be a viable approach to obtain novel extended CN networks with predetermined architectures.<sup>33</sup> Studies of the polymerization reactions of cyanogen,<sup>34</sup> cyanoacetylene,<sup>35</sup> tetracyanoethylene,<sup>36</sup> phosphorous tricyanide,<sup>37</sup> and acetonitrile<sup>38</sup> under pressure have helped to clarify the influences of starting materials and reaction conditions for the synthesis of new CN materials.

Dicyanoacetylene (C<sub>4</sub>N<sub>2</sub>) is a linear molecule with alternating triple and single bonds (N≡C-C≡C-C≡N).<sup>39</sup> The standard enthalpy of formation of C<sub>4</sub>N<sub>2</sub> is 500 kJ/mol,<sup>40</sup> leading to a flame temperature of over 5000 K.<sup>41</sup> Thus, C<sub>4</sub>N<sub>2</sub> represents an interesting, high-energy starting point to access novel extended CN networks. From the low-pressure side, people have examined C<sub>4</sub>N<sub>2</sub> and found reactions with benzene to produce aromatic hydrocarbons via the Diels-Alder reaction,<sup>42</sup> in addition to explosive decomposition into dinitrogen and graphite. Chien and Carlini synthesized polydicyanoacetylene via anionic polymerization of C<sub>4</sub>N<sub>2</sub> with *n*-butyllithium in THF, producing a linear polymer that cyclizes into a ladder polymer upon heating at 400 °C.<sup>42</sup> Interestingly, the physiochemical behavior of C<sub>4</sub>N<sub>2</sub> is also of astrophysical importance due to its presence in Titan's north polar stratosphere,<sup>44-47</sup> as detected by infrared spectroscopy. However, the interpretation of Raman and IR spectra is challenging, especially with regards to conflicting assignments for C≡N and C≡C stretching frequencies.<sup>48-54</sup> Inconsistencies between spectroscopic assignments for C<sub>4</sub>N<sub>2</sub> may arise from difficulties associated with sample preparation and handling due to its inherent instability and high reactivity; although it is of great importance for the understanding of intrinsic properties and conclusions regarding its detection.

To our knowledge, C<sub>4</sub>N<sub>2</sub> has not yet been examined under high-pressure conditions, which is of great interest from the perspective of novel carbon nitride materials and fundamental chemical

transformations. The large fraction of unsaturated bonds suggests potential for pressure-induced ring-forming reactions, as has been documented for a large number of other nitrile- and alkyne-based systems.<sup>34-38</sup> In addition,  $C_4N_2$  represents an interesting C:N stoichiometry to access extended networks with nitrogen content intermediate between typical deposition-based syntheses (nitrogen doping within a carbon framework) and precursor-based systems like graphitic  $C_3N_4$ . Moreover, high-pressure behavior can help to understand the nature of chemical bonding, reaction mechanisms, atomic structure and local environments of reaction products, which will advance the general understanding of carbon nitride materials.

Here, we study the high-pressure behavior of linear dicyanoacetylene ( $C_4N_2$ ) up to 10 GPa in diamond anvil cells. We first resolve the standing controversy regarding assignments of Raman and IR spectra, aided by first-principles phonon spectrum calculations. We next uncover a pressure-induced reaction process whereby discrete linear molecules polymerize into a disordered extended network without significant change to the bulk composition. This novel, amorphous material is fully recoverable to ambient conditions and its local structure, composition and chemical bonding was established using a variety of optical and X-ray scattering methods. The reaction mechanism was rationalized using molecular dynamics simulations. The present results provide a framework to further the understanding of the local mechanism of polymerization and offer valuable mechanistic insights into design guideline for the next-generation carbon nitride materials.

## METHODS

### *Synthesis*

$C_4N_2$  was prepared according to literature procedures.<sup>55</sup> All reactions were performed under an inert atmosphere of either nitrogen or argon. Diethyl ether was dried and deoxygenated over sodium-benzophenone ketyl prior to use. Sulfolane was purified by reaction with  $KMnO_4$  to remove alkene impurities, dried over KOH, and vacuum distilled prior to use.

**Acetylene dicarboxamide (1).** 100 mL of  $NH_3$  (4.8 mol) were condensed into a Schlenk flask and chilled to  $-78\text{ }^\circ\text{C}$ . Separately, 13.41 g (94.36 mmol) of dimethyl acetylenedicarboxylate (Sigma-Aldrich, 99%) were dissolved in 100 mL anhydrous diethyl ether ( $Et_2O$ ) and transferred dropwise to the chilled flask containing  $NH_3$ ; the reaction mixture quickly developed a red coloration. The reaction mixture was warmed to  $-45\text{ }^\circ\text{C}$  and stirred for 16 h at this temperature. Residual  $NH_3$  was boiled off at ambient temperature and the remainder was evaporated to dryness under vacuum, yielding a crude, orange product that was subsequently washed with cold ethanol. The resulting beige powder was recrystallized from 150 mL boiling ethanol at  $-20\text{ }^\circ\text{C}$ , yielding 8.27 g (78% yield) of white, crystalline solid after filtering and drying the powder under vacuum.

**Dicyanoacetylene (2).** 125 mL anhydrous sulfolane was added to a Schlenk flask equipped with a solids addition funnel and a secondary (detachable) vacuum trap. Using a mortar and pestle,

1  
2  
3 1.960 g (17.49 mmol) of acetylene dicarboxamide (**1**) was ground with 15.456 g (54.06 mmol)  
4 P<sub>2</sub>O<sub>5</sub> until homogeneous. Solids were added to the addition funnel, the apparatus was evacuated,  
5 the trap was chilled to -196 °C, and the sulfolane was heated to 110 °C with vigorous stirring.  
6 Solids were added slowly to the reaction mixture, which changed from colorless to yellow to red  
7 over time. After bubbling had ceased (~3 h), the trap containing the crude product was removed,  
8 transferred to an argon-filled glovebox, and liquid was pipetted into a small H-tube after melting.  
9 The liquid was frozen with LN<sub>2</sub>, a static vacuum of 50 mTorr was applied on the assembly. The  
10 dewar was transferred to the empty arm of the H-tube and the product was sublimed by warming  
11 the arm. The volatile, pale beige (almost colorless) liquid product was weighed within the  
12 glovebox at 0.794 g (60% yield). The product was stored at -35 °C under argon to prevent  
13 decomposition.  
14  
15  
16  
17  
18

19 **Poly-C<sub>4</sub>N<sub>2</sub>**. Liquid dicyanoacetylene (**2**) (~1 μl) was loaded into a ~150-210 μm diameter hole in  
20 a Re gasket using clean microsyringe. Before sample loading, Re gaskets were pre-indented to a  
21 thickness of 60-80 μm and mounted on 300-500 μm anvil culets of symmetric diamond anvil  
22 cells (DAC). Pressure was determined by measurement of fluorescence from a ruby standard  
23 placed inside the gasket hole.<sup>56</sup> To avoid any possible contamination of the highly reactive C<sub>4</sub>N<sub>2</sub>,  
24 a pressure medium was not used in the runs, but the molecular crystals are very soft and the  
25 influence of deviatoric stresses is expected to be small. All sample loadings were conducted in  
26 an inert Ar gas atmosphere glove box with oxygen and moisture concentrations of less than 1  
27 ppm. All samples were sealed to a starting pressure of ~0.1 GPa within the inert Ar atmosphere  
28 before removing from the glove box.  
29  
30  
31  
32

### 33 *Raman spectroscopy*

34  
35  
36 A system based around a Princeton Instruments spectrograph SP2750 (Trenton, NJ) with a 750  
37 mm focal length was used for the Raman spectra collections. A 532 nm diode laser was used as  
38 an excitation source and was focused through a 20× long working distance objective lens. The  
39 laser power was optimized to be ~1 mW and a short exposure time of ≤60 s was used to avoid  
40 local heating of the sample. Raman light was collected in the backscatter geometry through a 50  
41 μm confocal pinhole and two narrow-band notch filters (Ondax) were used to allow collection to  
42 within ~10 cm<sup>-1</sup> from the laser line. Raman light was collected through a 50 μm slit and dispersed  
43 off of an 1800 or 300 gr/mm grating onto a liquid nitrogen cooled charge coupled device (CCD)  
44 detector providing a spectral resolution of about 2 cm<sup>-1</sup>. The spectrometer was calibrated using  
45 the emission lines of Ne with an accuracy <1 cm<sup>-1</sup>.  
46  
47  
48  
49

### 50 *Infrared spectroscopy*

51  
52 Infrared transmission spectra were collected using a Varian 670-IR spectrometer system (Santa  
53 Clara, CA) utilizing a Globar source and KBr mid/near-IR beam splitter *ca.* 500-4000 cm<sup>-1</sup>.  
54 Infrared light was focused on and recollected through the sample using reflecting objective  
55 lenses. Transmitted light was collimated through a 50 μm pinhole for increased spatial resolution  
56  
57  
58  
59  
60

1  
2  
3 and passed to an HgCdTe detector. IR spectra were recorded at varying pressure. The same  
4 diamonds were used to obtain reference spectra after the cell was decompressed and cleaned.  
5  
6

### 7 *X-ray diffraction*

8  
9 Powder X-ray diffraction (XRD) measurements up to 13.0 GPa were collected in ~0.2 GPa  
10 pressure increments at the High Pressure Collaborative Access Team (HPCAT), beamline 16-  
11 IDB, of the Advanced Photon Source (APS), Argonne National Laboratory. A monochromatic  
12 beam ( $\sim 4 \times 5 \mu\text{m}^2$ ) with  $\lambda = 0.406626 \text{ \AA}$  was focused on the sample, and data were recorded  
13 using a MAR image plate. Diffraction images were processed using the FIT2D data analysis  
14 program.<sup>57</sup> Pressure was calibrated by the fluorescence from a Ruby sphere placed inside of the  
15 sample chamber.<sup>56</sup> The unit-cell volume and lattice parameters of  $\text{C}_4\text{N}_2$  were obtained through  
16 full profile fitting using the Le Bail<sup>58</sup> method, as implemented in GSAS with EXPGUI.<sup>59-60</sup>  
17  
18  
19

20  
21 Single-crystal X-ray diffraction studies for  $\text{C}_4\text{N}_2$  were carried out at the Advanced Photon Source,  
22 sector 16-BMD. Monochromatic X-rays ( $\lambda = 0.30998 \text{ \AA}$ ) with a beam size of ( $\sim 15 \times 30 \mu\text{m}^2$ )  
23 were focused on the sample and room-temperature diffraction was collected using a MAR image  
24 plate. The resulting data were processed and indexed using GSE-ADA/RSV.<sup>61</sup> Structure  
25 solutions and refinements were completed with the use of the SHELX-14 suite of programs.<sup>62-63</sup>  
26 Atom positions were standardized using the program STRUCTURE TIDY.<sup>64-65</sup> Crystallographic  
27 images were made using the program CRYSTALMAKER. Further crystallographic details can  
28 be found in the Supporting Information (SI) Table S1.  
29  
30  
31

32  
33 The structure factor of recovered amorphous  $\text{C}_4\text{N}_2$  was measured at the GSECARS 13-IDB  
34 beamline, Advanced Photon Source, ANL. The sample was measured with two different incident  
35 monochromatic X-ray beam energies: 25 keV ( $\lambda = 0.4959 \text{ \AA}$ ) for the low- $Q$  region and 60 keV ( $\lambda$   
36  $= 0.2066 \text{ \AA}$ ) for the high- $Q$  region. The beam sizes were  $2 \times 3 \mu\text{m}^2$  and  $4 \times 5 \mu\text{m}^2$ , respectively.  
37 Diffraction data were collected with a MAR345 image plate, whereby its position was calibrated  
38 using a  $\text{LaB}_6$  standard. Detector calibration, image integration and intensity correction for  
39 oblique X-ray-to-detector angle was performed using the Dioptas software package.<sup>66</sup> An empty  
40 Re-gasket with same thickness as the recovered sample was measured as background. The  
41 resulting data were stitched together from both measurements. The structure factor,  $S(Q)$ , and  
42 pair distribution function  $g(r)$  were calculated in the Faber-Ziman formalism. Data were  
43 collected up to a  $Q_{\text{max}}$  of  $17 \text{ \AA}^{-1}$ . The resulting data were optimized using a Kaplow-type  
44 correction<sup>67</sup> with three iterations. A Lorch modification function was used to remove unphysical  
45 oscillation in the resulting  $g(r)$ , which are a result of cutoff effects in the Fourier transformation.  
46 Density of the recovered sample was estimated by a method described by Eggert *et al.*<sup>68</sup>  
47  
48  
49  
50  
51

### 52 *Scanning Electron Microscopy*

53  
54  
55 The recovered samples within the Re gasket after Raman or Infrared spectral measurements were  
56 mounted on an Al rod holder for chemical composition mapping and microstructure observations  
57 using a field emission scanning electron microscope (FE-SEM; JEOL JSM 6500F) operating at  
58  
59  
60

1  
2  
3 15 kV and 1.5 nA. Compositional analyses were determined by energy-dispersive X-ray  
4 spectroscopy (EDS) using graphite and BN standards.  
5  
6

### 7 *Transmission Electron Microscopy and electron energy loss spectroscopy*

8

9  
10 TEM data collection and analysis were performed using both FEI Tecnai G2 LaB<sub>6</sub> and a FEI  
11 Talos F200X transmission electron microscopes (TEM). The samples were dispersed on a SiO  
12 grid with methanol and imaging was done under an accelerating voltage of 80 kV for both of the  
13 microscopes. Representative EDS data from the TEM were collected by a Bruker QUANTAX  
14 EDS system attached to the FEI TALOS TEM. Electron energy loss (EELS) / energy-filtered  
15 TEM measurements were carried out in diffraction mode under 80 kV using the Tecnai G2 LaB<sub>6</sub>.  
16 Carbon nano onions (CNOs) were used as a standard for pure 100% *sp*<sup>2</sup> carbon. Nascent REGAL  
17 250 carbon black was purchased from Cabot Corporation and graphitized at 3573 K for 5 hours  
18 to form highly crystalline CNOs.  
19  
20  
21

### 22 *X-ray Photoelectron spectroscopy*

23

24  
25 XPS experiments were performed using a Physical Electronics VersaProbe II instrument  
26 equipped with a monochromatic Al *k*<sub>α</sub> x-ray source (*hν* = 1,486.7 eV) and a concentric  
27 hemispherical analyzer. Charge neutralization was performed using both low-energy electrons  
28 (<5 eV) and Argon ions. The binding energy axis was calibrated using sputter-cleaned Cu foil  
29 (Cu 2p<sub>3/2</sub> = 932.7 eV, Cu 3p<sub>3/2</sub> = 75.1 eV). We assigned the pyridinic-N band in the N 1s spectra  
30 to the energy of 398.5 eV. Measurements were made at a takeoff angle of 45° with respect to the  
31 sample surface plane. This resulted in a typical sampling depth of 3-6 nm. Quantification was  
32 done using locally-derived sensitivity factors from a pure polyvinylpyrrolidone (PVP) reference  
33 sample. A soft surface cleaning was performed using 0.5 kV Ar<sup>+</sup>.  
34  
35  
36  
37

### 38 *TOF-SIMS*

39

40  
41 Time-of-flight secondary ion mass spectrometry (TOF-SIMS) analysis was performed using a  
42 Physical Electronics nanoTOF II instrument. A Bi<sub>3</sub><sup>2+</sup> primary ion beam with an ion dose of 5.0×  
43 10<sup>11</sup> ions/cm<sup>2</sup> was applied to an area of 100×100 μm<sup>2</sup> and negative secondary ions were collected.  
44 Charge compensation was performed using 10 eV Ar<sup>+</sup> and 12 eV electrons. The surface sputter  
45 cleaning was performed using 20 keV Ar<sub>2500</sub><sup>+</sup>. The sputtered area was 800×800 μm<sup>2</sup> with an ion  
46 dose of 5.0×10<sup>14</sup> ions/cm<sup>2</sup>. The melamine and highly oriented pyrolytic graphite (HOPG)  
47 analytical standards were purchased from Sigma-Aldrich and used without further purification.  
48  
49

### 50 *First-principles calculations*

51

52  
53 Ab initio molecular dynamics (AIMD) simulations for C<sub>4</sub>N<sub>2</sub> were performed within the *NPT* (*N*  
54 is the number of particles, *P* the pressure, and *T* the temperature) ensemble<sup>69</sup> implemented in  
55 Vienna ab Initio Simulation Package (VASP) code<sup>70</sup> with Langevin dynamics. The all-electron  
56 projector-augmented wave (PAW) potential<sup>71</sup> was adopted with the PAW potentials taken from  
57  
58  
59  
60

the VASP library where  $2s^22p^2$  and  $2s^22p^3$  are treated as valence electrons for C and N atoms, respectively. We generated  $2 \times 3 \times 3$  supercell of a conventional unit cell, containing 36 formula units (f. u.) in the simulation cell, which is big enough not to have a force field overlap with the nearest cells. The plane-wave was expanded to an energy cutoff of 400 eV and Brillouin zone sampling with a  $1 \times 1 \times 1$   $k$ -mesh were employed. Exchange and correlation effects were treated in the Perdew-Burke-Ernzerhof parameterization<sup>72</sup> of generalized gradient approximation. We also conducted Raman Intensity calculations using Quantum espresso software package<sup>73</sup> based on density functional perturbation theory<sup>74</sup>. Calculations for vibrational modes need highly accurate charge density and thus we carefully relaxed the atomic positions and the cell volume at a given external pressure. For the structural relaxation, we used a  $6 \times 8 \times 16$   $k$ -mesh with 700 eV energy cutoff and for Raman Intensity calculation we used a  $4 \times 6 \times 12$   $k$ -mesh with 700 eV energy cutoff.

## Results and Discussion

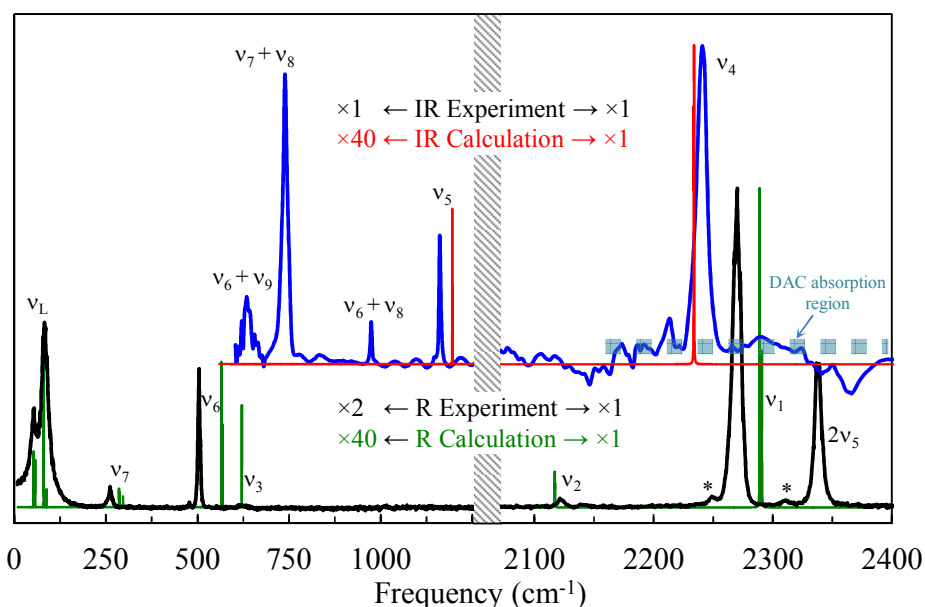


**Fig. 1.** Experimental and calculated Raman (bottom) and IR absorbance (top) spectra of solid  $C_4N_2$  at room temperature (RT) and 0.2 GPa. Calculated spectra are represented by Gaussian peak profiles with an arbitrary width. Spectral intensities are scaled by the factors indicated. Asterisks show contributions from  $^{13}C$  isotopologues. The thick dashed line in the IR spectrum indicates the diamond anvil absorption region.

### Molecular $C_4N_2$

$C_4N_2$  is a centrosymmetric linear molecule.<sup>39</sup> Consequently, it has  $3N-5=13$  fundamental vibrational modes, of which the Raman- and IR-active modes can be classified as  $\Gamma_{\text{Raman}} = 3\Sigma_g^+$  ( $\nu_1, \nu_2, \nu_3$ ) +  $2\Pi_g$  ( $\nu_6, \nu_7$ ) and  $\Gamma_{\text{IR}} = 2\Sigma_u^+$  ( $\nu_4, \nu_5$ ) +  $2\Pi_u$  ( $\nu_8, \nu_9$ ), given the molecule's  $D_{\infty h}$  symmetry. Raman and IR spectra of solid  $C_4N_2$  recorded at 0.2 GPa (the solidification pressure at RT) are shown in Fig.1. In order to provide accurate assignments of vibrational modes, we performed

density functional perturbation theory calculations, based on the previously-reported low-temperature crystal structure (confirmed under pressure, below),<sup>39</sup> to obtain vibrational mode frequencies and intensities. Experimentally, we observed all fundamental modes except the low-frequency IR-active bending modes ( $\nu_8$ ,  $\nu_9$ ), although we are able to infer their experimental frequencies based on observed combination bands. All experimental peak positions exhibit agreement with calculations within a frequency difference of 10%, allowing for accurate assignments.

Significant differences occur between previous mode assignments in the literature, notably in the high-frequency region and the distinction between  $\text{C}\equiv\text{N}$  and  $\text{C}\equiv\text{C}$  stretching.<sup>48-54</sup> Our observations indicate that the strongest Raman mode at 2270 ( $\nu_1$ )  $\text{cm}^{-1}$  can be assigned to  $\text{C}\equiv\text{N}$  symmetric stretching, although it is not a pure vibration and shows mixing with  $\text{C}\equiv\text{C}$  stretching character. The weaker intensity mode at 2122 ( $\nu_2$ )  $\text{cm}^{-1}$  is assigned to  $\text{C}\equiv\text{C}$  stretching. Previously, inconsistent assignments of the  $\text{C}\equiv\text{N}$  and  $\text{C}\equiv\text{C}$  stretching modes were made by Miller *et al.*<sup>48-49</sup> at 2290 and 2119  $\text{cm}^{-1}$ , Khanna *et al.*<sup>50</sup> at 2270 and 2331  $\text{cm}^{-1}$ , Smith *et al.*<sup>51</sup> at 2204 and 2224  $\text{cm}^{-1}$ , Winther *et al.*<sup>52</sup> at 2268 and 2121  $\text{cm}^{-1}$ , together with Bartel *et al.*<sup>54</sup> at 2296 and 2287  $\text{cm}^{-1}$ . Two extremely weak peaks at 2310 and 2138  $\text{cm}^{-1}$ , also previously observed at 2309 and 2137  $\text{cm}^{-1}$  by Miller *et al.*,<sup>48-49</sup> and 2307 and 2137  $\text{cm}^{-1}$  by Winther *et al.*,<sup>52</sup> correspond to the naturally abundant  $^{13}\text{C}$  isotopologue. The assignments of 618 ( $\nu_3$ ), 505 ( $\nu_6$ ) and 262 ( $\nu_7$ )  $\text{cm}^{-1}$  are consistent with previously reports as shown in Table I. Interestingly, two new lattice modes (83 and 51  $\text{cm}^{-1}$ ) are were observed for the first time in our Raman spectrum. The infrared spectrum of  $\text{C}_4\text{N}_2$  exhibits a strong peak at 2241( $\nu_4$ )  $\text{cm}^{-1}$ , corresponding to asymmetric  $\text{C}\equiv\text{N}$  and  $\text{C}\equiv\text{C}$  stretching modes. The observed mode at 1161 ( $\nu_5$ )  $\text{cm}^{-1}$  is appropriately assigned to be C-C asymmetric stretching. The strong mode at 2338  $\text{cm}^{-1}$  in the Raman spectrum is almost twice the frequency of this mode, which can be assigned to  $2\nu_5$ .

**Table I.** Observed and calculated Raman and IR modes.

		Experiment ( $\text{cm}^{-1}$ )	Theory ( $\text{cm}^{-1}$ )	Assignments
Raman	$\nu_1$ F. r.	2270	2290*	Symmetric $\text{C}\equiv\text{N}+\text{C}\equiv\text{C}$ stretching
Raman	$\nu_2$	2122	2117*	Symmetric $\text{C}\equiv\text{C}$ stretching
Raman	$\nu_3$	618	621*	Symmetric C-C stretching
IR	$\nu_4$	2241	2234*	Asymmetric $\text{C}\equiv\text{N}+\text{C}\equiv\text{C}$ stretching
IR	$\nu_5$	1161	1195*	Asymmetric C-C stretching
Raman	$\nu_6$	505	565*	C- $\text{C}\equiv\text{N}$ bending
Raman	$\nu_7$	262	285-296*	$\text{C}\equiv\text{C}-\text{C}$ bending
IR	$\nu_8$	477 <sup>#</sup>	509*	Bending
IR	$\nu_9$	129 <sup>#</sup>	120*	Bending

\*Most prominent frequency (theory predicts a number of modes of this character due to crystal field splitting); <sup>#</sup>Inferred from combinations. F.r. = Fermi resonance with  $2\nu_5$ .

The *in situ* behavior of  $C_4N_2$  was also studied under pressure to 13.0 GPa using single-crystal/powder X-ray diffraction. Single-crystal and powder XRD confirm that  $C_4N_2$  crystallizes in the same  $P2_1/c$  structure reported previously at low temperature.<sup>35</sup> The lattice parameters obtained at 0.2 GPa of  $a = 3.878(1) \text{ \AA}$ ,  $b = 6.058(1) \text{ \AA}$ ,  $c = 9.0262(2) \text{ \AA}$  and  $\beta = 98.94(3)^\circ$  are in good agreement with the low-pressure report (See SI, Tables S1-S2 and Fig.S1). With increasing pressure, the spectroscopic and diffraction data show that this structure is maintained to 5.5 GPa with a corresponding volume decrease of  $\sim 28\%$  (Fig.S2).

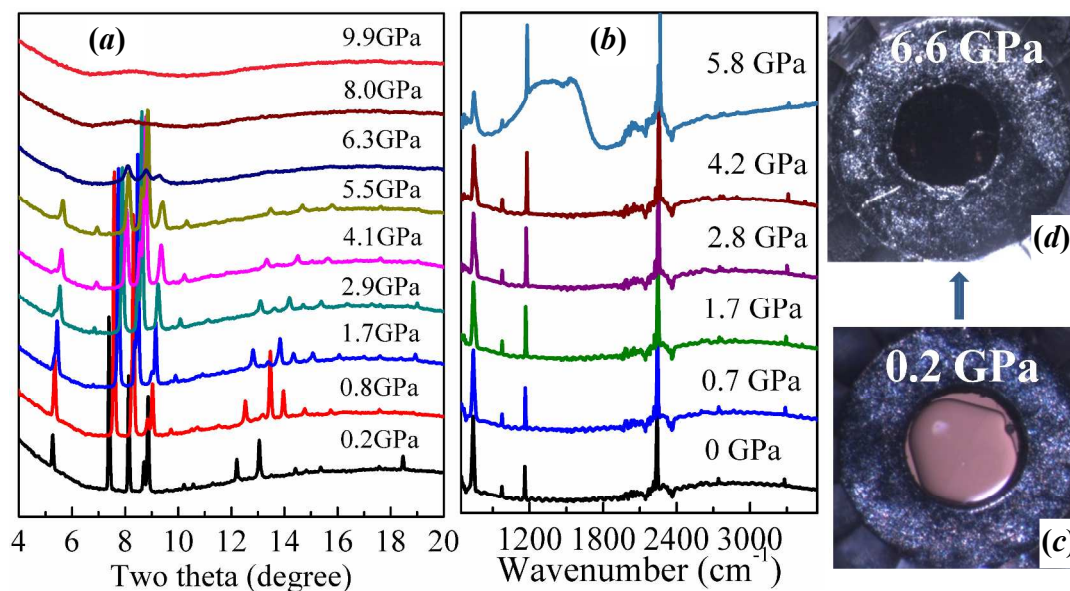


**Fig 2.** Representative (a) X-ray diffraction patterns, (b) IR spectra and (c-d) photos showing the onset of polymerization above  $\sim 6$  GPa.

### ***Polymerization into an extended network***

Above 5 GPa, changes in the Raman / IR spectra, as well as distinctive color changes of the sample, indicate the onset of a chemical transformation. The fundamental vibrational modes of  $C_4N_2$  decrease in intensity, while new, broad Raman/IR features (Fig.2b and Fig.S3 and S4) are observed near  $1200\text{--}1600 \text{ cm}^{-1}$ . Above 6 GPa the sample transforms from a transparent molecular crystal into a black and visibly opaque solid. Simultaneously, all crystalline diffraction is lost and only a diffuse halo remains visible in X-ray diffraction patterns (Fig 2). These features are indicative of the *sp* carbon and nitrogen reacting to form a disordered network with largely *sp*<sup>2</sup> character.

Upon releasing the pressure to ambient conditions, a solid phase with a black luster was recovered, in stark contrast to the transparent starting liquid phase, indicating the irreversibility of the chemical transformation. The morphology and composition of recovered phase was examined using SEM with compositional EDS mapping (Fig. 3a and Fig.S5). The recovered sample exhibits a smooth, uniform texture with homogenous chemical composition near 30 at%

nitrogen ( $C_4N_{1.8\pm 0.1}$ ). This composition indicates that the majority of nitrogen remains chemically bound within the sample with only a small degree of nitrogen loss, although EDS tends to overestimate carbon content due to various sources of carbon contamination.

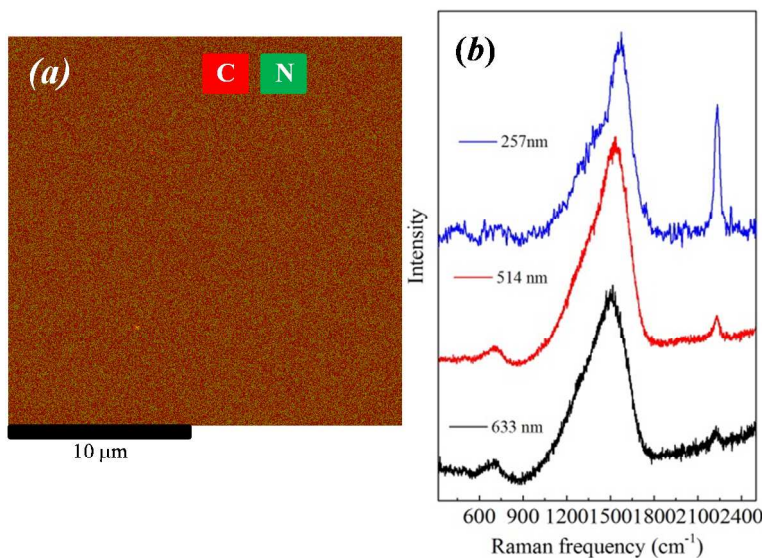


**Fig 3.** (a) Backscattered electron SEM image showing smooth morphology with overlaid EDS elemental mapping for recovered  $C_4N_2$ . The average composition was found to be  $C_4N_{1.8\pm 0.1}$ . (b) Multiwavelength Raman spectra of recovered samples.

Raman spectra from the recovered sample obtained at various laser excitation wavelengths are shown in Fig 3b. The spectra show three notable features, in contrast to the original spectra collected from the molecular crystal. A weak peak observed at 2222 ( $2227\text{ cm}^{-1}$ ) with 633 (514) nm indicates that a fraction of unconverted  $sp\ C\equiv N$  and/or  $C\equiv C$  bonding is preserved after the pressure-induced reaction. This  $sp$  vibration detected by UV Raman (257 nm) is much stronger than under visible excitation due to resonance enhancement, as also observed in previously amorphous carbon nitride thin film.<sup>87-90</sup> Broad Raman peaks are observed between 900-1800  $\text{cm}^{-1}$ , as previously observed for amorphous carbons or carbon nitrides.<sup>89-98</sup> These “D-” and “G-like” features are associated with  $C=N$  and/or  $C=C\ sp^2$  bonds and indicate the presence of disorder or a range of graphitic domains in the recovered material.<sup>87-90</sup> With increasing excitation wavelength, these broad peaks shift to lower wavenumber, similar to the  $G$  and  $D$  bands in amorphous carbon nitrides and carbon materials.<sup>97-98</sup> The peak at  $696\text{ cm}^{-1}$  with 633 nm excitation ( $700\text{ cm}^{-1}$  with 514 nm) is attributed to ring bending modes; this peak is barely visible in the UV Raman. We note that, due to overlap with the diamond  $T_{2g}$  phonon, combined with very weak Raman intensity above 6 GPa, we were not able to study the  $D$  and  $G$  features using Raman under in situ, high-pressure conditions.

### Structure of the recovered material

In order to gain deeper insights into the local structure of the recovered  $C_4N_2$ , we performed high-energy X-ray scattering experiments to obtain  $S(Q)$  to a momentum transfer of  $Q_{\max} = 17 \text{ \AA}^{-1}$ , and transformed this information into the radial distribution function,  $g(r)$ . In order to help interpret  $g(r)$ , we performed AIMD simulations at 12 GPa and 300 K, and relaxed the reaction product at ambient conditions. We note that a simulation pressure of 12 GPa was required to observe the rare event chemical reaction on time scales suitable for AIMD simulations. The obtained  $g(r)$  for the final disordered  $C_4N_2$  from both experiment and theory are shown in Fig. 4a. The  $g(r)$  derived from experiment yields an average first-neighbor distance of 1.36 Å, smaller than that of  $sp^2$  amorphous carbon (1.43-1.49 Å) and graphite (1.42 Å).<sup>87-88</sup> The calculated first-neighbor distance is 1.35 Å, which is very close to the experimental result. As suggested from Raman analysis, the recovered sample is dominated by  $sp^2$  C=C and C=N bonds. Compared with known C=C (1.42 Å in graphite and 1.399 Å in benzene) and C=N distances (1.30 Å in furazan, 1.33 Å in pyrazole, 1.34 Å in pyridine, 1.37 Å in pyrrole),<sup>87</sup> the average first-neighbor distance observed here also confirms that the dominant bonding contributions are from C=C and C=N bonds.

All general features of the experimental  $g(r)$  are reproduced by the calculations, suggesting that the calculated structure is a strong candidate to understand the polymeric structure of the disordered product. The structure consists of quasi-two-dimensional layers of  $sp^2$  rings that are sporadically connected by a fraction of  $sp^3$  carbon atoms (< 5%) (Fig. 4b). This extended polycyclic structure is comprised of mostly 5- and 6-membered rings, although a small fraction of rings with four and  $\geq 7$  members were also observed. The density estimate from the  $S(Q)$  and  $g(r)$  of the recovered material using the method of Eggert *et al.*<sup>67</sup> is  $2.12 \pm 0.1 \text{ g/cm}^3$ , compared with  $2.17 \text{ g/cm}^3$  from the MD simulation. These values are greater than  $2.0 \text{ g/cm}^3$  reported for CN(30% N),<sup>87</sup> but smaller than  $2.26 \text{ g/cm}^3$  for crystalline graphite. The calculated average C-C and C-N coordination numbers are 2.4 and 2.9, respectively. While 5% of the carbon atoms are 4-fold coordinated, a small fraction of unconverted  $sp$  and linear  $sp^2$  carbon keeps the average coordination number below three.

The second-nearest-neighbor peak in  $g(r)$  relates to the second coordination shell, and thus provides information on bond angles. Experimentally, this peak is located at 2.43 Å, which is slightly longer than 2.37 Å from calculations. These distances provide average bond angles of  $124.8^\circ$  and  $122.3^\circ$  for experiment and calculation, respectively, and indicate a disordered graphitic ring structure. The absence of any distinct features between 2.8-3.0 Å indicates that there is no significant fraction of ordered sixfold rings (the ideal cross-ring, 6-fold peak in graphite occurs at 2.84 Å).<sup>89</sup>

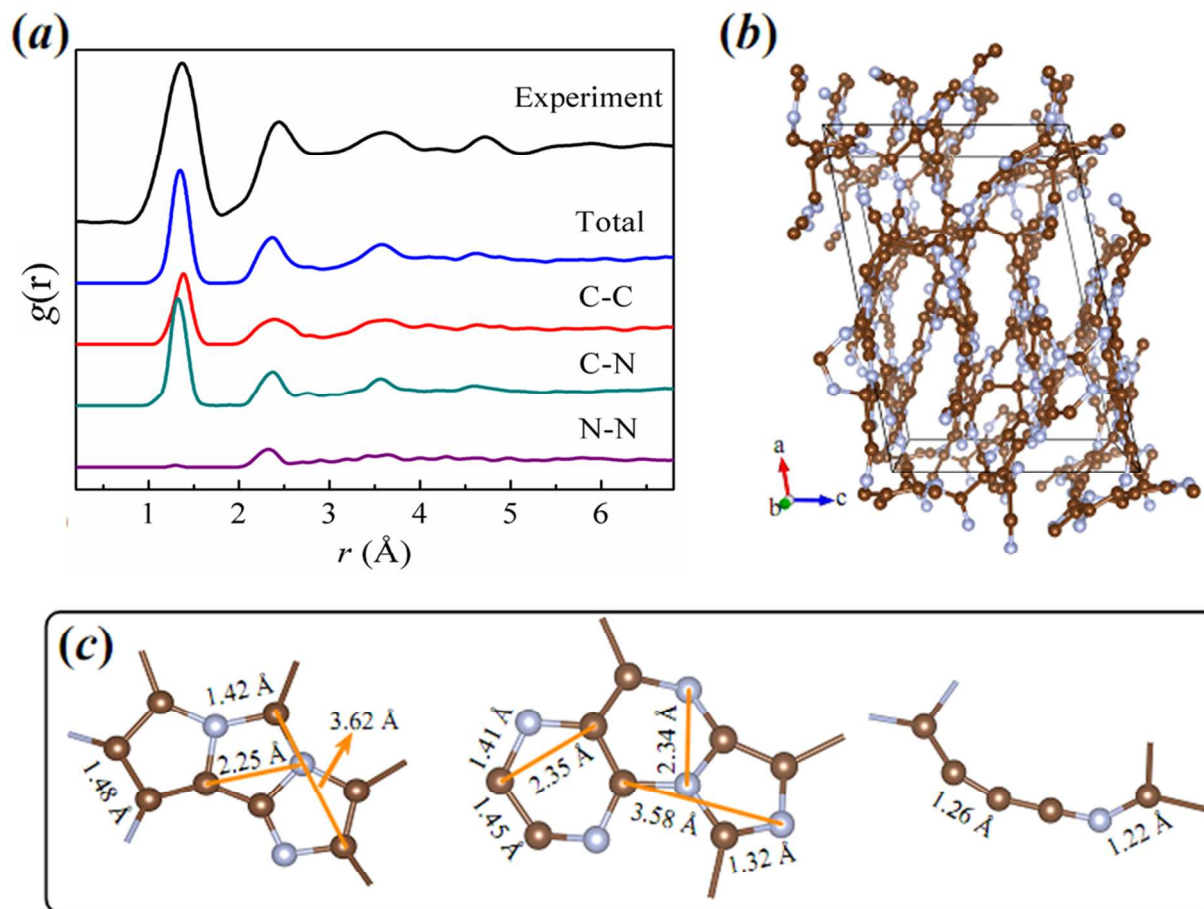


**Fig 4.** (a) Experimental and calculated  $g(r)$  including calculated partial correlations. (b) Relaxed MD structure showing CN network with tendency towards 2D layered structure. (c) Common local motifs with pyridinic- and pyrrolic-like characteristics and a fraction of partially reacted material.

### *X-ray photoelectron spectroscopy*

To provide additional information regarding the local structure and bonding features, we performed XPS measurements. The core-level XPS spectrum from the recovered sample is shown in Fig.5. The pristine recovered sample displays both carbon (C 1s) and nitrogen (N 1s) core-level peaks, in addition to a small oxygen contribution, resulting in the approximate chemical composition  $C_4N_{1.4}O_{0.24}$ . We confirmed that the bulk interior of the sample did not contain any oxygen by performing a soft  $Ar^+$  surface milling to remove  $\sim 0.5$  Å of material ( $\sim 20$  seconds at 0.5 kV), after which there was no detectable signal from the O 1s peak above the level of noise (Fig 5a). Thus, the oxygen signal originates from surface oxidation and does not exist within the bulk. After the surface cleaning, the chemical composition of the material indicated partial nitrogen loss ( $C_4N_{1.3}$ ), and we therefore conclude that the chemical composition of the recovered sample falls within the range of  $C_4N_{1.4\pm 0.1}$  based on XPS analysis, which is in general

1  
2  
3 agreement with the SEM-EDS composition. We note that both XPS (~26% N) and EDS (~31%  
4 N) analyses indicate partial nitrogen loss as compared with the starting molecular  $C_4N_2$ , but both  
5 techniques typically bias carbon due to environmental (adventitious) surface sources, and thus  
6 we consider  $C_4N_{1.4\pm 0.1}$  as a lower bound on the actual nitrogen concentration. Due to the  
7 observed nitrogen loss after  $Ar^+$  milling, which suggests possible alteration of the local chemical  
8 structure, we chose to analyze the raw XPS data, before cleaning. We note, however, that there  
9 were no major differences between the spectra obtained before and after milling, aside from  
10 minor changes in relative peak intensities (and the obvious absence of oxygen).

11  
12  
13  
14  
15 The carbon nitride literature contains numerous and varying reports concerning the interpretation  
16 of XPS spectra.<sup>90-109</sup> XPS spectra provide information regarding the binding energies of core-  
17 level electrons, which are a function of local environment including coordination number and  
18 nearest-neighbor constituents. To a first approximation, partial charge, *e.g.*, how much electron  
19 density is withdrawn by neighbors, can be used to generalize trends in binding energies. All  
20 other factors being equal, a  $sp^2$  carbon bound to another carbon atom will possess a lower  
21 binding energy than a  $sp^2$  carbon bound to an oxygen atom. In well-ordered molecular or  
22 crystalline systems, it is often straightforward to assign observed binding energies to specific  
23 sites, given sufficient spectral resolution. Yet, in disordered materials, such as the recovered  
24  $C_4N_2$  presented here, numerous local environments exist, and spectra should be considered in a  
25 statistical manor. Because we do not have sufficient spectral resolution to observe all possible  
26 local chemical environments, we employed the following approach to understand the measured  
27 XPS spectra. All XPS spectra were processed by first subtracting a linear background function.  
28 A series of trial peak functions was tested for each energy region and it was determined that  
29 simple Gaussian peak profiles could sufficiently describe the spectra as well as more complex  
30 functions using the fewest number of adjustable parameters. We used the minimum number of  
31 Gaussian peaks needed to adequately fit each spectrum, and each peak within the same binding  
32 energy region was constrained to have the same FWHM. Using this approach we can  
33 qualitatively understand the prominent local environments present within the recovered samples.

34  
35  
36  
37  
38  
39  
40  
41  
42 The N 1s core-level region (Fig. 5b) was deconvoluted into two different Gaussian components  
43 located at 398.5 and 400.3 eV, which are consistent with the general N 1s features reported for  
44 amorphous carbon nitride and N-doped graphene.<sup>90-109</sup> The most intense feature at 398.5 eV is  
45 attributed to “pyridinic-type” local environments, whereas the less-intense feature at 400.3 eV is  
46 attributed to “pyrrolic-type” environments. We note that, while this nomenclature is common in  
47 the XPS literature, these terms do not explicitly mean pyridine or pyrrole, but refer to whether  
48 the nitrogen lone pair participates in the  $\pi$  system.<sup>90-112</sup> We were unable to resolve the small  
49 contribution from unreacted nitrile groups, or any fraction of  $sp^3$  nitrogen atoms. Analysis of  
50 structures produced by MD simulations indicates that approximately 46% of the N atoms can be  
51 classified as pyridinic (2-fold coordinated), 29% as pyrrolic (3-fold coordinated with short C=N  
52 bonds), 19% as  $sp^3$  (3-fold coordinated with long C-N bonds) and 6% as  $sp$ . The remaining  
53 nitrile nitrogen likely contributes towards the “pyridinic” XPS contribution observed at low  
54  
55  
56  
57  
58  
59  
60

binding energy, whereas, the 3-fold coordinate N atoms with long bonds likely contribute more towards the “pyrrolic” contribution at higher binding energy. Adding these together from calculation, the pyridinic+ $sp$  and pyrrolic+ $sp^3$  contributions are roughly 50% each, compared with 69(5)% and 31(5)% averaged over four independent experimental observations. These features are in general agreement, but we note again that it was not possible to precisely describe all expected N 1s chemical environments in the peak fitting.<sup>90,100</sup>

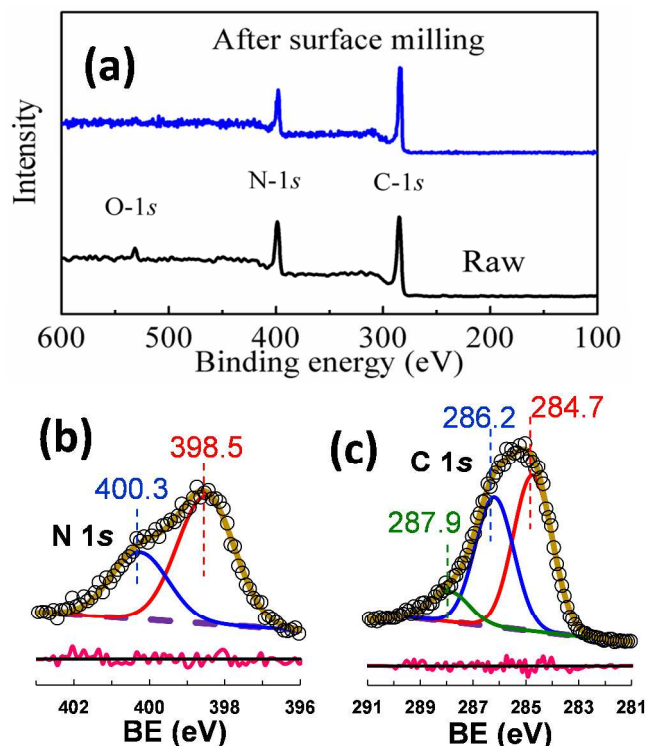


**Fig 5.** (a) XPS survey for recovered sample before and after ion milling. (b) Representative N 1s and (c) C 1s XPS spectra of the raw surface before ion milling.

The C 1s core-level spectrum (Fig. 5c) is characterized by a broad peak, tailing towards higher binding energy, which is evidence for high  $sp^2$  carbon content in the material.<sup>90-109</sup> The spectrum could be described by three Gaussian components at 284.7, 286.2 and 287.9 eV. The highest BE peak is attributed to C=O bonds on the surface and is expected on the basis of a weak O 1s peak in the survey scan. For  $sp^2$  dominated carbon materials, The XPS literature generally assigns the low BE peak near 284.7 eV to C=C bonds and the higher 286.2 eV peak to C=N bonds.<sup>93,100</sup> But this assignment is incomplete and the real situation is more complex. Nearly every carbon atom in the recovered material is 3-fold coordinated, thus the identity of these three neighbors is needed for a base-level interpretation, *e.g.*, CCC, CCN, CNN, NNN. Our MD simulations reveal no NNN environments, while approximately 39 % of 3-coordinated carbon atoms are CNN, 52% are CCN and 9% are CCC. Experimentally, the peaks at 287.7 eV and 286.2 eV comprise 52(7)%

1  
2  
3 and 48(7)% of the C 1s signal, respectively, when averaged over four independent observations  
4 (discounting the contribution of oxygen). Thus, the 284.7 eV peak could represent predominantly  
5 CCC and CCN environments, while the 286.2 eV peak could represent CNN environments.  
6 While the interpretations across experiment and theory are fully consistent (MD:  
7 CCC+CCN=61%; CNN=39%, experiment: CCC+CCN=52(7)%; CNN=48(7)%), we must  
8 emphasize that we cannot fully resolve all C 1s chemical environments. A small fraction of  $sp^3$   
9 carbon and unreacted nitrile carbon will also contribute to the overall shape of the XPS spectrum,  
10 although the  $sp^2$  features will dominate.  
11  
12  
13  
14

### 15 *Transmission electron microscopy*

16  
17 High-resolution TEM, together with selected-area electron diffraction (Fig 6), confirms that the  
18 material lacks long-range order, in agreement with the X-ray diffraction results. The TEM and  
19 EELS measurements were carried out using low beam energy with short acquisition times in  
20 order to minimize potential sample damage. HRTEM (Fig 6b) indicates that the material has a  
21 smooth texture at the atomic scale and no local domains of order are present. In addition, STEM-  
22 EDS mapping (Fig 6c, d) of the recovered sample confirms that carbon and nitrogen are distributed  
23 homogeneously with no signs of chemical disproportionation. The full-range EELS spectrum  
24 exhibits the characteristic 1s to  $\sigma^*$  and 1s to  $\pi^*$  transitions in both the carbon and nitrogen K-  
25 edge regions, similar to previous measurements of  $CN_x$  films.<sup>102</sup> Zooming in on these regions  
26 (Fig 6 e, f), the sample shows an abundance of  $sp^2$  bonding in the carbon and nitrogen atoms, as  
27 indicated by the presence of 1s peaks at both C and N K-edge. The  $sp^2$ -content was calculated to  
28 be  $\sim 90 \pm 5\%$  using graphitized carbon nano-onions as a standard using the method proposed by  
29 Brydson *et al.*<sup>110</sup>  
30  
31  
32  
33  
34  
35  
36  
37  
38  
39  
40  
41  
42  
43  
44  
45  
46  
47  
48  
49  
50  
51  
52  
53  
54  
55  
56  
57  
58  
59  
60

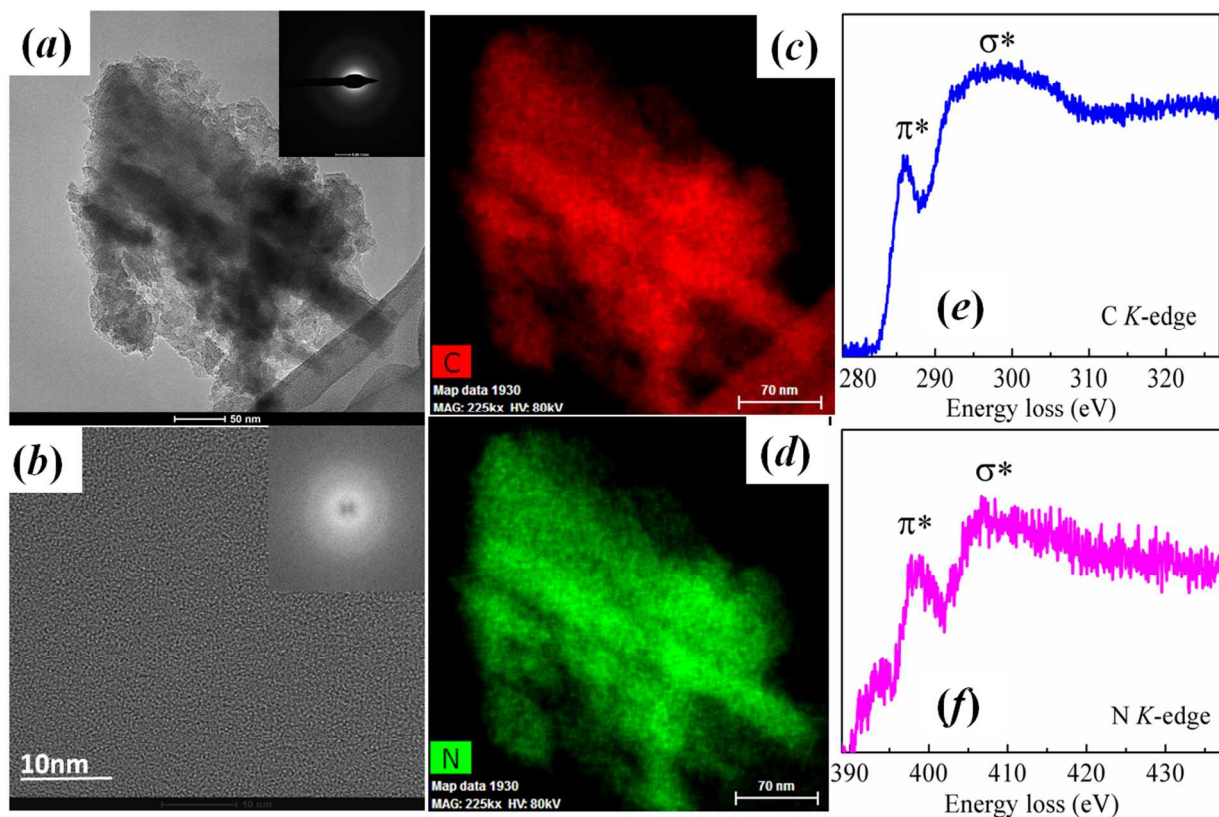


**Fig. 6.** (a) Obtained TEM with diffraction pattern (inset), (b) HRTEM with fast Fourier transformation (inset), elemental analysis of (c) C and (d) N, and EELS of (e) carbon and (f) nitrogen *K* edges for recovered sample of  $C_4N_2$ .

### Mass Spectrometry

In order to further study the structure of the disordered carbon nitride, we carried out time-of-flight secondary ion mass spectrometry measurements (TOF-SIMS). The sample surface was cleaned using 20 keV  $Ar_{2500}^+$  ion sputtering to remove signals from surface contaminants and to reveal the true characteristics of the bulk material. The mass spectra of graphitic materials, such as highly oriented pyrolytic graphite (HOPG), do not contain monomeric molecular ions owing to their extended structure. However, graphitic surfaces do exhibit characteristic fragmentation patterns in the negative ion spectrum that consist of a series of prominent  $C_xH_y$  peaks with low hydrogen content.<sup>112</sup> The negative ion spectrum of HOPG (as shown in Fig. S6) exhibits features associated with  $C^-$ ,  $CH^-$ ,  $C_2^-$ ,  $C_2H^-$ ,  $C_3^-$ ,  $C_4^-$ ,  $C_5^-$ , and  $C_6^-$ . These prominent features indicate a low hydrogen content and a fragmentation pattern consistent with an extended carbon structure (2D graphite in this case). The negative ion spectrum for recovered  $C_4N_2$  is presented in Fig. 7, together with the table of major fragments. In this case, the most prominent fragments are C-N ions (such as  $CN^-$ ,  $C_3N^-$ ), C-C ions (such as  $C^-$ ,  $C_2^-$ ) and hydrogenated ions with low H content (such as  $CH^-$ ,  $C_2H^-$ ). Furthermore, larger  $C_xN_y$  fragments with high nitrogen content are also observed. These results confirm the formation of an extended carbon-nitrogen network

consisting predominantly of carbon-nitrogen and carbon-carbon bonds, and are similar to previously reported results for carbon nitride thin films.<sup>112</sup> In addition, the negative spectrum shows a similar fragmentation pattern to the TOF-SIMS spectrum of melamine, but with lower hydrogen content (Fig. S7). Compared with the spectrum of melamine, recovered  $C_4N_2$  shows similar low-mass ion fragmentation (*e.g.*,  $C^-$ ,  $CH^-$ ,  $C_2^-$ ,  $C_2H^-$ ,  $CN^-$ ,  $CN_2^-$ ,  $C_2N_3^-$ ), however, higher-mass protonated fragments such as  $CN_2H^-$ ,  $C_2N_3H^-$ ,  $C_2N_3H_2^-$  are far less prominent.

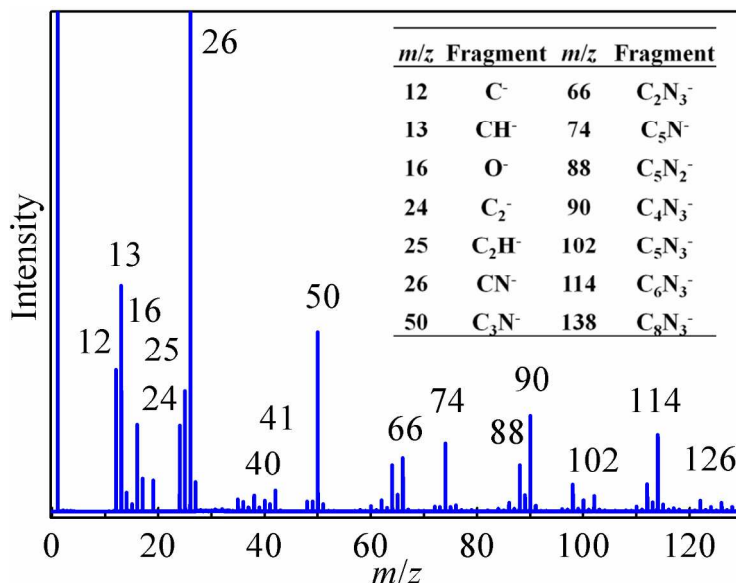


**Fig. 7.** The TOF-SIMS negative ion spectrum of the sample after  $Ar_{2500}^+$  ion sputtering.  $C_xN_y$  fragments with low content of hydrogen were observed. Although the hydrocarbon contamination on the surface is largely removed by ion sputtering, the contamination is still detected. However, the  $C_xN_y$  fragments peaks are prominent and therefore provides a direct evidence of an extended carbon-nitrogen network presented. The negative fragment ions are listed.

### Polymerization mechanism

Previously reported static *ab initio* calculations suggest that below 14 GPa, there are no thermodynamically stable crystalline carbon nitride phases<sup>113</sup> including graphitic  $C_3N_4$ <sup>114</sup> and its modified allotropes<sup>115</sup>. Here we work in the realm of metastability and examined potential reaction pathways of crystalline, molecular  $C_4N_2$  using a combination of molecular dynamics and metadynamics simulations, as well as evolutionary metadynamics,<sup>116</sup> as implemented in the USPEX code.<sup>117-118</sup> The former is intended to provide direct insights into the reaction mechanism, while the two versions of metadynamics are used to examine a larger portion of the potential energy landscape by overcoming rare-event barriers and to draw conclusions as the system evolves towards the ground state.

Molecular dynamics (NPT) trajectories were established from a supercell (36 molecules) of the starting  $P2_1/c$  structure at 300 K and 12 GPa. Initial polymerization was generally observed to occur within the first 2 ps of the run (the same polymerized structures were equilibrated at 0 GPa to obtain the  $g(r)$  data in Fig. 4). The molecular structure can be viewed as two-dimensional sheets of  $C_4N_2$  molecules that lie in a single plane when viewed approximately normal to the (201) direction (Fig. 8). Within these sheets, side-aligned columns of  $C_4N_2$  molecules propagate down the  $b$ -axis. Two types of columns exhibit ABAB stacking within the  $\sim(201)$  plane where the A column is canted by  $\sim 67^\circ$  with respect to the B column. The shortest interatomic distance in the starting structure is between the nitrile nitrogen of a molecule in column A and the nitrile carbon atom of an adjacent molecule in column B ( $\sim 3.3$  Å at 1 atm).

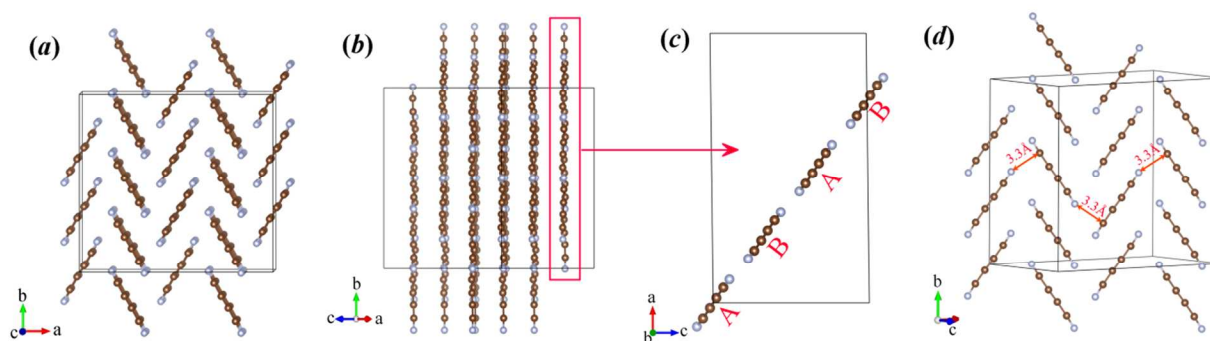


**Fig. 8.** (a) Molecular structure of  $C_4N_2$ . (b) View approximately normal to the (201) direction. (c) Molecules form columns along the  $b$ -axis with ABAB stacking. (d) The shortest distance between columns is 3.3 Å at 1 atm.

When compressed to 12 GPa, the linear  $C_4N_2$  molecules began to kink. Some of the  $C-C\equiv C$  and  $N\equiv C-C$  angles drop to as low as  $140^\circ$  within the first 2 ps, indicating enhanced interactions between neighboring molecules. As expected from the starting crystal structure, the initial polymerization initiates between the shortest  $N\cdots C$  distance within a single 2D “sheet”. The polymerization proceeds within individual sheets through cycloaddition reactions that produce predominantly 5- and 6-membered rings, giving the overall structure a tendency to propagate in two dimensions. Over time, unreacted bonds begin to form connections between the 2D layers, producing a more interconnected structure that still remains largely two-dimensional. Ultimately, the final disordered  $C_4N_2$  structure is unchanged after  $\sim 20$  picoseconds. This process is summarized in Figure 9.

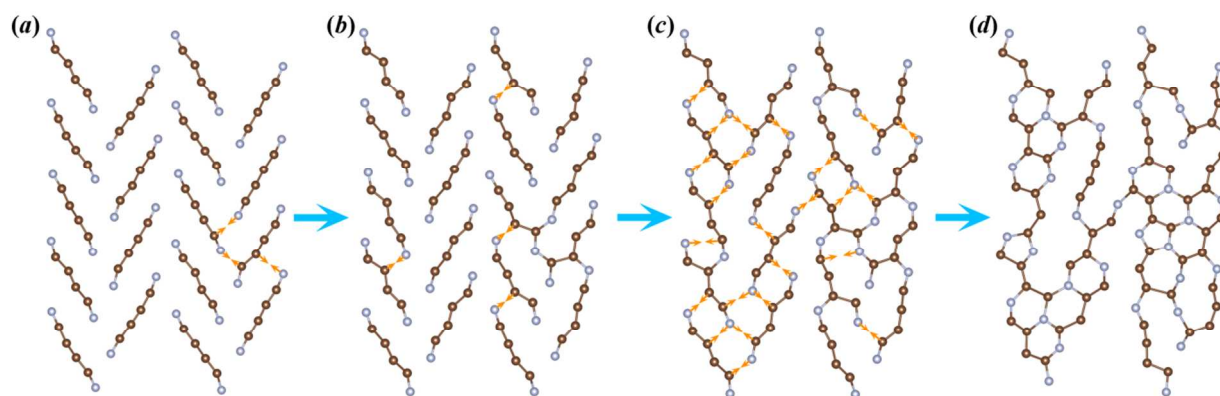


**Fig.9.** Polymerization process of  $C_4N_2$  at 12 GPa and 300K shown at (a) 1.8 ps, (b) 2.0 ps, (c) 2.1 ps and (d) 2.4 ps. Orange arrows indicate reaction points.

At 300K, MD trajectories become essentially trapped within a single configuration after polymerization occurs – there is not enough energy relative to  $kT$  for the probable observation of rare-event, covalent-bond breaking at our simulation timescales. In order to gain insights into the tendency of the system to evolve over longer time scales, we performed metadynamics simulations from the starting molecular structure (Fig.S8). The metadynamics algorithm uses scaled components of the edge vectors of the simulation cell as collective variables. The driving force that guides the evolution of the simulation cell is the derivative of the Gibbs free energy with respect to the six collective variables, which were updated in every meta-step toward a low-energy pathway to neighboring minima. In our metadynamics simulation,  $C_4N_2$  ultimately transformed to a two-dimensional layered structure. The final layered structure has a very low symmetry with the space group of  $P1$ , which can be understood as an approximate amorphous structure. The structural evolutions and calculated  $g(r)$  for the  $P1$  structure and the experimental data are shown in the supporting information (Fig. S9). The metadynamics reaction sequence and calculated  $g(r)$  are very similar when compared with the MD simulations, confirming the mechanism of the reaction process and the general tendency during the polymerization of  $C_4N_2$  is towards a two-dimensional structure comprised of heterocyclic rings. Interestingly, the evolutionary metadynamics simulations also revealed low-energy 2D and 3D crystalline structures, as reported in the supplementary material. These structures are reported in the Fig.S11 and S12 and represent interesting future targets for metastable synthesis.

## CONCLUSIONS

In summary, by starting with a hydrogen-free  $C_4N_2$  molecular precursor, an amorphous extended carbon nitride with similar composition can be synthesized via high-pressure, solid-state chemistry. The fundamental vibrational modes of the molecular precursor were also definitively assigned with the help of DFT calculations. The recovered product is a largely two-dimensional polycyclic network comprised of predominantly three-fold coordinated  $sp^2$  carbon with “pyrrolic-“ and “pyridinic-like” nitrogen. A small fraction of  $sp^3$  carbon connects disordered 2D

1  
2  
3 layers in three dimensions. The reaction proceeds by the activation of linear C<sub>4</sub>N<sub>2</sub> molecules into  
4 buckled chains that spontaneously assemble through cycloaddition reactions. This understanding  
5 of the high-pressure behavior and polymerization mechanism of C<sub>4</sub>N<sub>2</sub> will provide fundamental  
6 contributions to carbon nitride chemistry.  
7  
8

## 11 ASSOCIATED CONTENT

### 13 Supporting Information

16 The Supporting Information is available free of charge on the ACS Publications website at DOI.

18 Single-crystal X-ray diffraction analysis, Raman and infrared spectra with pressure, SEM-EDS  
19 data, TOF-SIMS data, metadynamics structures.  
20  
21

## 23 ACKNOWLEDGEMENTS

25 This work was supported by DARPA under ARO Contract No. W31P4Q-13-I-0005. Portions of  
26 this work were performed at HPCAT (Sector 16), Advanced Photon Source (APS), Argonne  
27 National Laboratory. HPCAT operations are supported by DOE-NNSA under Award No. DE-  
28 NA0001974 and DOE-BES under Award No. DE-FG02-99ER45775, with partial  
29 instrumentation funding by NSF. Portions of this work were also carried out at  
30 GeoSoilEnviroCARS (The University of Chicago, Sector 13), Advanced Photon Source (APS),  
31 Argonne National Laboratory. GeoSoilEnviroCARS is supported by the National Science  
32 Foundation - Earth Sciences (EAR-1128799) and Department of Energy-GeoSciences (DE-  
33 FG02-94ER14466). This research used resources of the Advanced Photon Source, a U.S.  
34 Department of Energy (DOE) Office of Science User Facility operated for the DOE Office of  
35 Science by Argonne National Laboratory under Contract No. DE-AC02-06CH11357. H.G.  
36 acknowledges financial support from the National Natural Science Foundation of China (NSFC)  
37 under Grants No. 51201148 and U1530402, as well as the Thousand Youth Talents Plan. D.Y.K.  
38 acknowledges the Texas Advanced Computing Center (TACC) at the University of Texas at  
39 Austin and Argonne Leadership Computing Facility (ALCF) which is a DOE Office of Science  
40 User Facility supported under Contract No. DE-AC02-06CH11357 for providing high  
41 performance computing resources.  
42  
43  
44  
45  
46  
47  
48

## 49 REFERENCES

- 51  
52 (1) Liu, A.Y.; Cohen, M. L. Prediction of new low compressibility solids. *Science* **1989**,  
53 245, 841-842.  
54 (2) Teter, D. M.; Hemley, R. J. Low-compressibility carbon nitrides. *Science* **1996**, 271, 53-55.  
55 (3) Niu, C.; Lu, Y. Z.; Lieber, C. M. Experimental realization of the covalent solid carbon nitride.  
56 *Science* **1993**, 261, 334-337.  
57  
58  
59  
60

- 1  
2  
3 (4) Badding, J. V. Solid-state carbon nitrides. *Adv. Mater.* **1997**, *9*, 877-886.
- 4 (5) Thomas, A.; Fischer, A.; Goettmann, F.; Markus Antonietti, M.; Müller, J. F.; Robert  
5 Schlögl, Carlsson, J. M. Graphitic carbon nitride materials: variation of structure and  
6 morphology and their use as metal-free catalysts. *J. Mater. Chem.* **2008**, *18*, 4893-4908.
- 7 (6) Wang, X.; Maeda, K.; Thomas, A.; Takanabe, K.; Xin, G.; Carlsson, J. M.; Domen, K.;  
8 Antonietti, M. A metal-free polymeric photocatalyst for hydrogen production from water under  
9 visible light. *Nature Mater.* **2009**, *8*, 76-80.
- 10 (7) Liu, G.; Niu, P.; Sun, C.; Smith, S. C.; Chen, Z.; Lu, G.; Cheng, H. M. Unique electronic  
11 structure induced high photoreactivity of sulfur-doped graphitic C<sub>3</sub>N<sub>4</sub>. *J. Am. Chem. Soc.* **2010**,  
12 *132*, 11642-11648.
- 13 (8) Wang, Y.; Wang, X.; Antonietti, M. Polymeric graphitic carbon nitride as a heterogeneous  
14 organocatalyst: from photochemistry to multipurpose catalysis to sustainable chemistry. *Angew.*  
15 *Chem. Int. Ed.* **2012**, *51*, 68-89.
- 16 (9) Zheng, Y.; Liu, J.; Liang, J.; Jaroniec, M.; Qiao, S. Graphitic carbon nitride materials:  
17 controllable synthesis and applications in fuel cells and photocatalysis. *Energy Environ. Sci.*,  
18 **2012**, *5*, 6717-6731.
- 19 (10) Li, X. H.; Antonietti, M. Metal nanoparticles at mesoporous N-doped carbons and carbon  
20 nitrides: functional Mott-Schottky heterojunctions for catalysis. *Chem. Soc. Rev.* **2013**, *42*, 6593-  
21 6604.
- 22 (11) Zhu, J.; Xiao, P.; Li, H.; Carabineiro, S. A. C. Graphitic carbon nitride: synthesis, properties,  
23 and applications in catalysis. *ACS Appl. Mater. Interfaces* **2014**, *6*, 16449-16465.
- 24 (12) Zhao, Z.; Sun, Y.; Dong, F.; Graphitic carbon nitride based nanocomposites: a review.  
25 *Nanoscale* **2015**, *7*, 15-37.
- 26 (13) Cao, S.; Low, J.; Yu, J.; Jaroniec, M. Polymeric photocatalysts based on graphitic carbon  
27 nitride. *Adv. Mater.* **2015**, *27*, 2150-2176.
- 28 (14) Zheng, Y.; Lin, L.; Wang, B.; Wang, X. Graphitic carbon nitride polymers toward  
29 sustainable photoredox catalysis. *Angew. Chem. Int. Ed.* **2015**, *54*, 12868-12884.
- 30 (15) Liu, J.; Wang, H.; Antonietti, M. Graphitic carbon nitride “reloaded”: emerging  
31 applications beyond (photo) catalysis. *Chem. Soc. Rev.* **2016**, *45*, 2308-2326.
- 32 (16) Ong, W. J.; Tan, L.; Ng, Y. H.; Yong, S. T.; Chai, S. P. Graphitic carbon nitride (g-C<sub>3</sub>N<sub>4</sub>)-  
33 based photocatalysts for artificial photosynthesis and environmental remediation: are we a step  
34 closer to achieving sustainability? *Chem. Rev.* **2016**, *116*, 7159-7329.
- 35 (17) Patnaik, S.; Satyabadi, M.; Saumyapraava, A.; Parida, K. M. An overview of the  
36 modification of g-C<sub>3</sub>N<sub>4</sub> with high carbon containing materials for photocatalytic applications.  
37 *Inorg. Chem. Front.* **2016**, *3*, 336-347.
- 38 (18) Kang, Y.; Yang, Y.; Yin, L.; Kang, X.; Liu, G.; Cheng, H. Efficient C<sub>3</sub>N<sub>4</sub>/graphene oxide  
39 macroscopic aerogel visible-light photocatalyst. *Adv. Mater.* **2015**, *27*, 4572-4577.
- 40 (19) Fan, J.; Chen, J.; Zhang, Q.; Chen, B.; Zang, J.; Zheng, M.; Dong, Q. An Amorphous  
41 Carbon Nitride Composite Derived from ZIF-8 as Anode Material for Sodium-Ion Batteries.  
42 *ChemSusChem* **2015**, *8*, 1856-1861.
- 43 (20) Sjostrom, H.; Hultman, L.; Sundgren, J. E.; Hainsworth, S. V.; Page, T. F.; Theunissen, G.  
44 Structural and mechanical properties of carbon nitride CN<sub>x</sub> (0.2 ≤ x ≤ 0.35) films. *J. Vac. Sci.*  
45 *Technol. A* **1996**, *14*, 56-62.
- 46 (21) Hellgren, N.; Johansson, M. P.; Broitman, E.; Hultman, L.; Sundgren, J. E. Role of nitrogen  
47 in the formation of hard and elastic CN<sub>x</sub> thin films by reactive magnetron sputtering. *Phys. Rev.*  
48 *B* **1999**, *59*, 5162-5169.
- 49  
50  
51  
52  
53  
54  
55  
56  
57  
58  
59  
60

- 1  
2  
3 (22) Holloway, B. C.; Kraft, O.; Shuh, D. K.; Nix, W. D.; Kelly, M. A.; Pianetta, P.; Hagstrom, S.  
4 Interpretation of x-ray photoelectron spectra of elastic amorphous carbon nitride thin films. *Appl.*  
5 *Phys. Lett.* **1999**, *74*, 3290-3292.
- 6 (23) Wan, L.; Egerton, R. F. Preparation and characterization of carbon nitride thin films. *Thin*  
7 *Solid Films* **1996**, *279*, 34-42.
- 8 (24) Spaeth, C.; Kuhn, M.; Richter, F.; Falke, U.; Hietschold, M.; Kilper, R.; Kreissig, U. A  
9 comparative study of elastic recoil detection analysis (ERDA), electron energy loss spectroscopy  
10 (EELS) and X-ray photoelectron spectroscopy (XPS) for structural analysis of amorphous carbon  
11 nitride films. *Diamond Relat. Mater.* **1998**, *7*, 1727-1733.
- 12 (25) Zheng, W. T.; Yu, W. X.; Li, H. B.; Wang, Y. M.; Cao, P. J.; Jin, Z. S.; Broitman, E.;  
13 Sundgren, J. E. Chemical bonding, structure, and hardness of carbon nitride thin films. *Diamond*  
14 *Relat. Mater.* **2000**, *9*, 1790-1794.
- 15 (26) Gammon, W. D.; Malyarenko, I.; Kraft, O.; Hoatson, G. L.; Reilly, A. C.; Holloway, B.C.  
16 Hard and elastic amorphous carbon nitride thin films studied by <sup>13</sup>C nuclear magnetic resonance  
17 spectroscopy. *Phys. Rev. B* **2002**, *66*, 153402:1-4.
- 18 (27) Zhang, Z.; Leinenweber, K.; Bauer, M.; Laurence A. J. Garvie, L. A. J.; McMillan, P. F.;  
19 Wolf, G. H. High-Pressure Bulk Synthesis of Crystalline C<sub>6</sub>N<sub>9</sub>H<sub>3</sub>•HCl: A Novel C<sub>3</sub>N<sub>4</sub> Graphitic  
20 Derivative. *J. Am. Chem. Soc.*, **2001**, *123*, 7788-7796.
- 21 (28) Jurgens, B.; Irran, E.; Serker, J.; Kroll, P.; Muller, H.; Schnick, W. Melem (2, 5, 8-triamino-  
22 tri-s-triazine), an important intermediate during condensation of melamine rings to graphitic  
23 carbon nitride: Synthesis, structure determination by X-ray powder diffractometry, solid-state  
24 NMR, and theoretical studies. *J. Am. Chem. Soc.*, **2003**, *125*, 10288-10300.
- 25 (29) Lotsch B.V.; Schnick, W. Thermal conversion of guanylurea dicyanamide into graphitic  
26 carbon nitride via prototype CN<sub>x</sub> precursors. *Chem. Mater.*, **2005**, *17*, 3976-3982.
- 27 (30) Lotsch B. V.; Schnick, W. From Triazines to Heptazines: Novel Nonmetal  
28 Tricyanomelaminates as Precursors for Graphitic Carbon Nitride. *Chem. Mater.* **2006**, *18*, 1891-  
29 1900.
- 30 (31) Horvath-Bordon, E., Riedel, R., McMillan, P. F., Kroll, P., Mieke, G., van Aken, P. A.;  
31 Zerr, A.; Hoppe, P.; Shebanova, O.; McLaren, I.; Lauterback, S.; Kroke, E.; Boehler, R. High-  
32 Pressure Synthesis of Crystalline Carbon Nitride Imide, C<sub>2</sub>N<sub>2</sub>(NH). *Angew. Chem. Int.*  
33 *Edit.* **2007**, *46*, 1476-1480.
- 34 (32) Salamat, A.; Deifallah, M.; Carbrera, R.Q.; Cora, R.; McMillan, P. F. Identification of new  
35 pillared-layered carbon nitride materials at high pressure. *Sci. Rep.* **2013**, *3*, 2122:1-6.
- 36 (33) Schettino, V.; Bini, R. Molecules under extreme conditions: Chemical reactions at high  
37 pressure. *Phys. Chem. Chem. Phys.* **2003**, *5*, 1951-1965.
- 38 (34) Yoo, C. S.; Nicol, M. F. Chemical and phase transformations of cyanogen at high  
39 pressures. *J. Phys. Chem.* **1986**, *90*, 6726-6731.
- 40 (35) Aoki, K.; Kakudate, Y.; Yoshida, M.; Usuba, S.; Fujiwara, S. Solid state polymerization of  
41 cyanoacetylene into conjugated linear chains under pressure. *J. Chem. Phys.* **1989**, *91*, 778-782.
- 42 (36) Tomasino, D.; Chen, J. Y.; Minesob Kim, M.; Yoo, C. S. Pressure-induced phase transition  
43 and polymerization of tetracyanoethylene (TCNE). *J. Chem. Phys.* **2013**, *138*, 094506:1-10.
- 44 (37) Gou, H.; Yonke, B. L.; Epshteyn, A.; Kim, D. K.; Smith, J. S.; Strobel T. A. Pressure-  
45 induced polymerization of P(CN)<sub>3</sub>. *J. Chem. Phys.* **2015**, *142*, 194503:1-9.
- 46  
47  
48  
49  
50  
51  
52  
53  
54  
55  
56  
57  
58  
59  
60

- 1  
2  
3 (38) Zheng, H.; Li, K.; Cody, G.; Tulk, C. A.; Dong, X.; Gao, G.; Molaison, J. J.; Liu, Z.;  
4 Feyngenson, M.; Yang, W.; Ivanov, I. N.; Basile, L.; Idrobo, J. C.; Guthrie, M.; Mao, H. K. Phase  
5 Transitions and Polymerization of C<sub>6</sub>H<sub>6</sub>-C<sub>6</sub>F<sub>6</sub> Co-crystal under Extreme Conditions. *Angew.*  
6 *Chem. Int. Ed.* **2016**, *55*, 2040-2044.
- 7  
8 (39) Hanan, R. B.; Collin, R. L. The crystal structure of dicyanoacetylene. *Acta Cryst.* **1953**, *6*,  
9 350-352.
- 10 (40) Armstrong, G.T.; Marantz, S. The Heat of Combustion of Dicyanoacetylene. *J. Phys. Chem.*  
11 **1963**, *67*, 2888
- 12 (41) Kirshenbaum, A. D.; Grosse, A. V. The combustion of carbon subnitride, C<sub>4</sub>N<sub>2</sub>, and a  
13 chemical method for the production of continuous temperatures in the range of 5000-6000° K. *J.*  
14 *Am. Chem. Soc.*, **1956**, *78*, 2020.
- 15 (42) Ciganek, E. Diels-Alder additions of dicyanoacetylene to aromatic hydrocarbons.  
16 *Tetrahedron Lett.* **1967**, *8*, 3321-3325.
- 17 (43) Chien, J. C. W.; Carlini, C. Semiconducting poly(dicyanoacetylenes). *J. Polym. Sci.: Polym.*  
18 *Chem. Edt.* **1985**, *23*, 1383-1393.
- 19 (44) Coll, P.; Guillemine, J. C.; Gazeau, M. C.; Raulin, F. Report and implications of the first  
20 observation of C<sub>4</sub>N<sub>2</sub> in laboratory simulations of Titan's atmosphere. *Planet. Space Sci.* **1999**, *47*,  
21 1433-1440.
- 22 (45) Nishio, M.; Paillous, P.; Khlifi, M.; Bruston, P.; Raulin, F. Infrared spectra of gaseous  
23 ethanenitrile in the 3500-250 cm<sup>-1</sup> region: absolute band intensity and implications for the  
24 atmosphere of Titan. *Spectrochimica Acta* **1995**, *51A*, 617-622.
- 25 (46) Samuelson, R. E.; Mayo, L. A.; Knuckles, M. A.; Khanna, R. J. C<sub>4</sub>N<sub>2</sub> ice in Titan's north  
26 polar stratosphere. *Planet. Space Sci.* **1997**, *45*, 941-948.
- 27 (47) de Kok, R. J.; Teanby, N. A.; Maltagliati, L.; Irwin, P. G. J.; Vinatier, S. HCN ice in Titan's  
28 high-altitude southern polar cloud. *Nature* **2014**, *514*, 65-67.
- 29 (48) Miller, F. A.; Hannan, Jr. R. B. The Infrared and Raman Spectra of Dicyanoacetylene. *J.*  
30 *Chem. Phys.* **1953**, *21*, 110-114.
- 31 (49) Miller, F. A.; Hannan, Jr. R. B.; Cousins, L. R. Infrared and Raman Spectra of  
32 Dicyanoacetylene. II. *J. Chem. Phys.* **1955**, *23*, 2127-2129.
- 33 (50) Khanna, R. K.; Perera-Jarmer, M. A.; Ospina, M. J. Vibrational infrared and Raman spectra  
34 of dicyanoacetylene. *Spectrochimica Acta.* **1987**, *43A*, 421-425.
- 35 (51) Smith, A. M.; Schallmoser, G.; Thoma A.; Bondybey, V. E. Infrared spectral evidence of  
36 N≡C-C≡C-N≡C: Photoisomerization of N≡C-C≡C-N≡C in an argon matrix. *J. Chem. Phys.* **1993**,  
37 *98*, 1776-1785.
- 38 (52) Winther, F.; Schonhoff, M. The Fundamental Vibrations of N≡C-C≡C-N≡C  
39 (Dicyanoacetylene). *J. Mol. Spectrosc.* **1997**, *186*, 54-65.
- 40 (53) Khlifi, M.; Paillous, P.; Bruston, P.; Guillemin, J. C.; Benilan, Y.; Daoudi, A.; Raulin, F.  
41 Gas infrared spectra, assignments, and absolute IR band intensities of C<sub>4</sub>N<sub>2</sub> in the 250-3500 cm<sup>-1</sup>  
42 region: implications for Titan's stratosphere. *Spectrochimica Acta* **1997**, *53A*, 707-712.
- 43 (54) Bartel, C.; Botschwina, P.; Bürger, H.; Guarnieri, A.; Heyl, A.; Huckauf, A.; Lentz, D.;  
44 Merzliak, T.; Mkadmi, E. B. Cyanoisocynoacetylene, N≡C-C≡C-N≡C. *Angew. Chem. Int. Ed.*  
45 **1998**, *37*, 2879-2882.
- 46 (55) Saggiomo, A. J. The Dinitriles of Acetylenedicarboxylic and Polyacetylenedicarboxylic  
47 Acids. I. 2 Dicyanoacetylene and Dicyanodiacetylene. *J. Org. Chem.*, **1957**, *22*, 1171-1175.
- 48  
49  
50  
51  
52  
53  
54  
55  
56  
57  
58  
59  
60

- 1  
2  
3  
4  
5  
6  
7  
8  
9  
10  
11  
12  
13  
14  
15  
16  
17  
18  
19  
20  
21  
22  
23  
24  
25  
26  
27  
28  
29  
30  
31  
32  
33  
34  
35  
36  
37  
38  
39  
40  
41  
42  
43  
44  
45  
46  
47  
48  
49  
50  
51  
52  
53  
54  
55  
56  
57  
58  
59  
60
- (56) Mao, H. K.; Xu, J.; Bell, P. M. Calibration of the ruby pressure gauge to 800 kbar under quasi-hydrostatic conditions. *J. Geophys. Res.* **1986**, *91*, 4673-4676.
- (57) Hammersley, A. P.; Svensson, S. O.; Hanfland, M.; Fitch, A. N.; Häsermann, D. Two-dimensional detector software: from real detector to idealized image or two-theta scan. *High Pressure Res.* **1996**, *14*, 235-248.
- (58) Le Bail, A. ESPOIR: a program for solving structures by Monte Carlo from powder diffraction data. *Mater. Sci. Forum* **2001**, 378-381, 65-70.
- (59) Larson, A. C.; Von Dreele, R. B. Los Alamos National Lab. Report **2000**, LAUR 86-748.
- (60) Desgreniers, S.; Lagarec, K. XRDA3.1-a program for X-ray diffraction analysis on a PC. *J. Appl. Crystallogr.* **1998**, *31*, 109-110.
- (61) Dera, P.; Zhuravlev, K.; Prakapenka, V.; Rivers, M. L.; Finkelstein, G. J.; Grubor-Urosevic, O.; Tschauner, O.; Clark, S. M.; Downs, R. T. High pressure single-crystal micro X-ray diffraction analysis with GSE\_ADA/RSV software. *High Pressure Research* **2013**, *33* (3), 466-484.
- (62) Sheldrick, G. A short history of SHELX. *Acta Crystallogr. Section A* **2008**, *64* (1), 112-122.
- (63) Sheldrick, G. Crystal structure refinement with SHELXL. *Acta Crystallogr. Section C* **2015**, *71* (1), 3-8.
- (64) Parthe, E.; Gelato, L. M. The standardization of inorganic crystal-structure data. *Acta Crystallogr. Section A* **1984**, *40* (3), 169-183.
- (65) Gelato, L. M.; Parthe, E. STRUCTURE TIDY—a computer program to standardize crystal structure data. *J. Applied Crystallogr.* **1987**, *20* (2), 139-143.
- (66) Prescher, C.; Prakapenka, V. B. DIOPTAS: a program for reduction of two-dimensional X-ray diffraction data and data exploration. *High Press. Res.* **2015**, *35*, 223-230.
- (67) Eggert, J.; Weck, G.; Loubeyre, P.; Mezouar, M. Quantitative structure factor and density measurements of high-pressure fluids in diamond anvil cells by x-ray diffraction: Argon and water. *Phys. Rev. B* **2002**, *65*, 174105-174116.
- (68) Kaplow, R.; Strong, S. L.; Averbach, B. L. Radial density functions for liquid mercury and lead. *Phys. Rev.* **1965**, *138*, A1336-1345.
- (69) Hernández, E. Metric-tensor flexible-cell algorithm for isothermal–isobaric molecular dynamics simulations. *J. Chem. Phys.* **2001**, *115*, 10282-10290.
- (70) Kresse, G.; Furthmüller, J. Efficient iterative schemes for ab initio total-energy calculations using a plane-wave basis set. *Phys. Rev. B* **1996**, *54*, 11169-11186.
- (71) Kresse, G.; Joubert, D. From ultrasoft pseudopotentials to the projector augmented-wave method. *Phys. Rev. B* **1999**, *59*, 1758-1775.
- (72) Perdew, J. P.; Burke, K.; Ernzerhof, M. Generalized gradient approximation made simple. *Phys. Rev. Lett.* **1996**, *77*, 3865-3868.
- (73) Giannozzi, P.; Baroni, S.; Bonini, N. *et al.* QUANTUM ESPRESSO: a modular and open-source software project for quantum simulations of materials. *J. Phys.: Condens. Matter* **2009**, *21*, 395502:1-19.
- (74) Baroni, S.; de Gironcol, S.; Dal Corso, A.; Giannozzi, P. Phonons and related crystal properties from density-functional perturbation theory. *Rev. Mod. Phys.* **2001**, *73*, 515-562.
- (75) Ferrari, A. C.; Robertson, J. Origin of the 1150 cm<sup>-1</sup> Raman mode in nanocrystalline diamond. *Phys. Rev. B* **2001**, *63*, 121405:1-4.
- (76) Ferrari, A. C.; Rodil, S. E.; Robertson, J. Interpretation of infrared and Raman spectra of amorphous carbon nitrides. *Phys. Rev. B.* **2003**, *67*, 155306:1-20.

- 1  
2  
3  
4 (77) Ferrari, A. C.; Rodil, S. E.; Robertson, J. Resonant Raman spectra of amorphous carbon  
5 nitrides: the G peak dispersion. *Diamond and Related Mater.* **2003**, *12*, 905-910.
- 6 (78) Ferrari, A. C.; Robertson, J. Raman spectroscopy of amorphous, nanostructured, diamond-  
7 like carbon, and nanodiamond. *Phil. Trans.R. Soc.Lond. A:* **2004**, *362*, 2477-2512.
- 8 (79) Rodil, S. E.; Muhl, S. Bonding in amorphous carbon nitride. *Diamond and Related Mater.*  
9 **2004**, *13*, 1521-1531.
- 10 (80) Tamor, M. A.; Wu, C. H. Graphitic network models of “diamondlike” carbon. *J. Appl. Phys.*  
11 **1990**, *67*, 1007-1012.
- 12 (81) Kaufman, J. H.; Metin, S.; Saperstein, D. D. Symmetry breaking in nitrogen-doped  
13 amorphous carbon: Infrared observation of the Raman-active G and D bands. *Phys. Rev. B*  
14 **1989**, *39*, 13053-13060.
- 15 (82) Beeman, D.; Silverman, J.; Lynds, R.; Anderson, M. R. Modeling studies of amorphous  
16 carbon. *Phys. Rev. B* **1984**, *30*, 870-875.
- 17 (83) Shi, J. R.; Shi, X.; Sun, Z.; Liu, E.; Tay, B. K.; Lau, S. P. Ultraviolet and visible Raman  
18 studies of nitrogenated tetrahedral amorphous carbon films. *Thin Solid Films* **2000**, *366*, 169-174.
- 19 (84) Ferrari, A. C.; Robertson, J. Interpretation of Raman spectra of disordered and amorphous  
20 carbon. *Phys. Rev. B* **2000**, *61*, 14095-14107.
- 21 (85) Ferrari, A. C.; Robertson, J. Resonant Raman spectroscopy of disordered, amorphous, and  
22 diamondlike carbon. *Phys. Rev. B* **2001**, *64*, 075414:1-13.
- 23 (86) Casari, C. S.; Li Bassi, A.; Baserga, A.; Ravagnan, L.; Piseri, P.; Lenardi, C.; Tommasini,  
24 M.; Milani, A.; Fazzi, D.; Bottani, C. E.; Milani, P. Low-frequency modes in the Raman  
25 spectrum of  $sp$ - $sp^2$  nanostructured carbon. *Phys. Rev. B* **2008**, *77*, 195444-1:7.
- 26 (87) Walters, J. K.; Kühn, M.; Spaeth, C.; Fischer, H.; Richter, F.; R. J. Newport. Neutron-  
27 diffraction studies of amorphous  $CN_x$  materials. *Phys. Rev. B* **1997**, *56*, 14315-14320
- 28 (88) Clark, S. J.; Crain, J.; Ackland, G. J. Comparison of bonding in amorphous silicon and  
29 carbon. *Phys. Rev. B* **1997**, *55*, 14059-14062.
- 30 (89) Li, F.; Lannin, J. S. Radial distribution function of amorphous carbon. *Phys. Rev. Lett.* **1990**,  
31 *65*, 1905-1908.
- 32 (90) Titantah, J.T.; Lamoen, D. Carbon and nitrogen 1s energy levels in amorphous carbon  
33 nitride systems: XPS interpretation using first-principles. *Diamond Related Mater.* **2007**, *16*, 581-  
34 588.
- 35 (91) Bartle, K. D.; Perry, D. L.; Wallace, S. The functionality of nitrogen in coal and derived  
36 liquids: an XPS study. *Fuel Process. Technol.* **1987**, *15*, 351-361.
- 37 (92) Kelemen, S. R.; Gorbaty, M. L.; Kwiatek, P. J. Quantification of nitrogen forms in Argonne  
38 premium coals. *Energy & Fuels.* **1994**, *8*, 896-906.
- 39 (93) Hellgrena, N.; Haaschb, R. T.; Schmidt, S.; Hultman, L.; Petrov, I. Interpretation of X-  
40 ray photoelectron spectra of carbon-nitride thin films: New insights from in situ XPS. *Carbon*  
41 **2016**, *108*, 242-252.
- 42 (94) E D'Anna, E.; De Giorgi, M.L.; Luches, A.; Martino, M.; Perrone, A.; Zocco, A. Study of  
43 C-N binding states in carbon nitride films deposited by reactive XeCl laser ablation. *Thin Solid*  
44 *Films* **1999**, *347*, 72-77.
- 45 (95) Ech-chamikh, E.; Essafti, A.; Ijdiyaou, Y.; Azizan, M. XPS study of amorphous carbon  
46 nitride (aC:N) thin films deposited by reactive RF sputtering. *Solar Energy Mater. Solar Cells*  
47 **2006**, *90*, 1420-1423.
- 48  
49  
50  
51  
52  
53  
54  
55  
56  
57  
58  
59  
60

- 1  
2  
3  
4  
5  
6  
7  
8  
9  
10  
11  
12  
13  
14  
15  
16  
17  
18  
19  
20  
21  
22  
23  
24  
25  
26  
27  
28  
29  
30  
31  
32  
33  
34  
35  
36  
37  
38  
39  
40  
41  
42  
43  
44  
45  
46  
47  
48  
49  
50  
51  
52  
53  
54  
55  
56  
57  
58  
59  
60
- (96) Pels, J. R.; Kapteijn, F.; Moulijn, J. A.; Zhu, Q.; Thomas, K. M. Evolution of nitrogen functionalities in carbonaceous materials during pyrolysis. *Carbon* **1995**, *33*, 1641-1653.
- (97) Estrade-Szwarckopf, H. XPS photoemission in carbonaceous materials: A “defect” peak beside the graphitic asymmetric peak. *Carbon* **2004**, *42*, 1713-1721.
- (98) Zheng, W. T.; Xing, K. Z.; Hellgrena, N.; Lögdlanda, M.; Johanssona, Å.; Gelivsb, U.; Salanecka, W.R.; Sundgrena, J.-E. Nitrogen 1s electron binding energy assignment in carbon nitride thin films with different structures. *J. Electron Spectros. Rel. Phenom.* **1997**, *87*, 45-49.
- (99) Hellgren, N.; Johansson, M. P.; Broitman, E.; Hultman, L.; Sundgren, J. E. Role of nitrogen in the formation of hard and elastic CN<sub>x</sub> thin films by reactive magnetron sputtering. *Phys. Rev. B* **1999**, *59*, 5162-5169.
- (100) Ronning, C.; Feldermann, H.; Merk, R.; Hofsass, H.; Reinke, P.; Thiele, J. U. Carbon nitride deposited using energetic species: a review on XPS studies. *Phys. Rev. B* **1998**, *58*, 2207-2215.
- (101) Ripalda, J. M.; Román, E.; Díaz, N.; Galán, L.; Montero, I.; Comelli, G.; Baraldi, A.; Lizzit, S.; Goldoni, A.; Paolucci, G. Correlation of X-ray absorption and X-ray photoemission spectroscopies in amorphous carbon nitride. *Phys. Rev. B* **1999**, *60*, 3705-3708.
- (102) Braun, A.; Huggins, F.E.; Shah, N.; Chen, Y.; Wirick, S.; Mun, S.B.; Jacobsen, C.; Huffman, G.P. Advantages of soft X-ray absorption over TEM-EELS for solid carbon studies—a comparative study on diesel soot with EELS and NEXAFS. *Carbon* **2005**, *43*, 117-124.
- (103) Qu, L.; Liu, Y.; Baek, J.; Dai, L. Nitrogen-doped graphene as efficient metal-free electrocatalyst for oxygen reduction in fuel cells. *ACS Nano*, **2010**, *4*, 1321-1321
- (104) Geng, D.; Chen, Y.; Chen, Y.; Li, Y.; Li, R.; Sun, X.; Ye, S.; Knights, S. High oxygen-reduction activity and durability of nitrogen-doped grapheme. *Energy Environ. Sci.* **2011**, *4*, 760-764.
- (105) Wang, H.; Maiyalagan, T.; Wang, X. Review on recent progress in nitrogen-doped graphene: synthesis, characterization, and its potential applications. *ACS Catal.* **2012**, *2*, 781-794
- (106) Warner, J. H.; Lin, H. C.; He, K.; Koshino, M.; Suenaga, K. Stability and spectroscopy of single nitrogen dopants in graphene at elevated temperatures. *ACS Nano*, **2014**, *8*, 11806-11815.
- (107) Arenal, R.; March, K.; Ewels, C. P.; Rocquefelte, X.; Kociak, M.; Loiseau, A.; Stephan, O. Atomic configuration of nitrogen-doped single-walled carbon nanotubes. *Nano lett.* **2014**, *14*, 5509-5516
- (108) Lin, Y.; Teng, P.; Yeh, C.; Koshino, M.; Chiu, P.; Suenaga, K. Structural and chemical dynamics of pyridinic-nitrogen defects in grapheme. *Nano lett.* **2015**, *15*, 7408-7413.
- (109) Gupta, N. K.; Peng, B.; Haller, G. L.; Ember, E. E.; Lercher, J. A. Nitrogen Modified Carbon Nano-Materials as Stable Catalysts for Phosgene Synthesis. *ACS Catal.* **2016**, *6*, 5843-5855.
- (110) Brydson, R.; Zhili, Z.; Brown, A. Revisiting the determination of carbon sp<sup>2</sup>/sp<sup>3</sup> ratios via analysis of the EELS carbon K-edge. *Vol. 1: Instrumentation and Methods* **2008**, *12*, 357-358.
- (111) Deslandes, A.; Jasieniak, M.; Ionescu, M.; Shapter, J. G.; Fairman, C.; Gooding, J. J.; Quinton, J. S. ToF SIMS characterisation of methane and hydrogen plasma modified graphite using principal component analysis. *Surface and Interface Analysis* **2009**, *41*, 216-224.

- 1  
2  
3  
4  
5  
6  
7  
8  
9  
10  
11  
12  
13  
14  
15  
16  
17  
18  
19  
20  
21  
22  
23  
24  
25  
26  
27  
28  
29  
30  
31  
32  
33  
34  
35  
36  
37  
38  
39  
40  
41  
42  
43  
44  
45  
46  
47  
48  
49  
50  
51  
52  
53  
54  
55  
56  
57  
58  
59  
60
- (112) Huang, L. J.; Hung, Y.; Chang, S.; Massoumi, G. R.; Lennard, W. N.; Mitchell, I. V. Characterization of carbon and carbon nitride thin films using time-of-flight secondary-ion-mass spectrometry. *J. Vacuum Science Technology a-Vacuum Surfaces and Films* **1997**, *15*, 2196-2201.
- (113) Dong, H.; Oganov, A.R.; Zhu, W.; Qian, G. Prediction of a new ground state of superhard compound B<sub>6</sub>O at ambient conditions. *Sci. Rep.* **2016**, *5*, 9870-9874.
- (114) Kroke, E. gt-C<sub>3</sub>N<sub>4</sub>-The First Stable Binary Carbon (IV) Nitride, *Angew. Chem., Int. Ed.* **2014**, *53*, 11134-11135.
- (115) Pickard, C. J.; Salamat, A.; Bojdys, M. J.; Needs, R. J.; McMillan, P. F. Carbon nitride frameworks and dense crystalline polymorphs. *Phys. Rev. B* **2016**, *94*, 094104:1-10.
- (116) Zhu, Q.; Oganov, A.R.; Lyakhov, A.O. Evolutionary metadynamics: a novel method to predict crystal structures. *Cryst. Eng. Comm.* **2012**, *14*, 3596-3601.
- (117) Oganov, A.R., Glass, C.W. Crystal structure prediction using ab initio evolutionary techniques: Principles and applications. *J. Chem. Phys.* **2006**, *124*, 244704.
- (118) Lyakhov, A.O.; Oganov, A.R.; Stokes, H.T.; Zhu Q. New developments in evolutionary structure prediction algorithm USPEX. *Comp. Phys. Comm.* **2013**. *184*, 1172-1182.

Table of Contents artwork

